The Bowland Shale Formation in the Blacon Basin: syngenetic processes, stacking patterns and heat productivity

Joseph F. Emmings[1,2,3]*, Jan A. I. Hennissen[1], Christopher H. Vane[1], Magret Damaschke[1], Lin Marvin[2], Vicky Moss-Hayes[1], Angela Lamb[1], Jack Lacey[1], Melanie J. Leng[1,4] and Nick J. Riley[5]

[1]British Geological Survey, Keyworth, Nottingham NG12 5GG, UK

[2]School of Geography, Geology and the Environment, University of Leicester, Leicester LE1 7RH, UK

[3]CGG, Tyn-y-Coed, Llanrhos, Llandudno LL30 1SA, UK

[4]Centre for Environmental Geochemistry, University of Nottingham, Leicestershire LE12 5RD, UK

[5]Carboniferous Limited, Glendevon, Selby Lane, Keyworth, Nottingham NG12 5AH, UK

JFE, 0000-0003-2084-0501

*Correspondence: joseph.emmings@cgg.com

Abstract: We conducted a high-resolution multi-disciplinary analysis of two core sections in the borehole Ellesmere Port-1, Cheshire, UK. Biostratigraphic analysis indicates that the core sections are Kinderscoutian and late Arnsbergian–Chokierian in age, respectively. Both cores are assigned to the Bowland Shale Formation (Holywell Shale). Coupled core scan and discrete geochemical analysis enables interpretation of syngenetic processes at a high stratigraphic resolution. Both cores exhibit the classic cyclicity of limestones, calcareous to non-calcareous mudstones and siltstones, interpreted to represent sediment deposition during fourth-order sea-level fluctuation. Machine learning of the well log data coupled to the core scan data enabled prediction of the key lithofacies through the entire Bowland Shale interval in Ellesmere Port-1. The machine predictions show that the Bowland Shale is interfingered with three turbiditic leaves of the Cefn-y-Fedw Sandstone Formation and contains at least 12 complete fourth-order cycles. The Bowland Shale exhibits high radiogenic heat productivity in comparison with other sedimentary rocks, due primarily to relative U enrichment under intermittently euxinic conditions. Thermal modelling, however, shows that the radiogenic heat productivity of the Bowland Shale contributes a negligible source of additional heat at the scale of hundreds of metres.

Supplementary material: Discrete bulk geochemical datasets (appendix A) , details of the calculations used Q2 for the heat flow box modelling (appendix B) and original TOC (appendix C) are available at https://doi.org/10.6084/m9.figshare.c.6911105

Organic and metal-rich mudstones, herein termed black shales, represent an important sedimentary rock type as archives of environmental perturbations (e.g. Wignall 1994; Algeo 2004; Meyer and Kump 2008; Kidder and Worsley 2010); sources and resources of hydrocarbons (e.g. Tissot and Welte 1984; Jarvie 2012*a*, *b*), ligands (e.g. Kendrick *et al.* 2002) and metals (e.g. Gadd *et al.* 2020); seals for injected CO_2 (e.g. Worden *et al.* 2020); and as sources of *in situ* sedimentary heat (e.g. Rybach 1976; Beardsmore *et al.* 2010). The UK Late Mississippian–Early Pennsylvanian Bowland Shale Formation represents a relatively thick black shale succession in the UK (e.g. Waters *et al.* 2007) with equivalent units in Europe (Kerschke and Schulz 2013; Zijp *et al.* 2017), and is a proven unconventional hydrocarbon resource in the UK (Andrews 2013; Clarke *et al.* 2018). Here we focus on the Bowland Shale Formation in the Ellesmere Port-1 well, drilled for unconventional hydrocarbons in 2014.

Palpable microseismicity (Clarke *et al.* 2019), uncertainty related to connectivity to shallow aquifers (e.g. Loveless *et al.* 2018) and recoverable hydrocarbons (Whitelaw *et al.* 2019) and overarching net-zero goals (e.g. IPCC 2014) suggest that the Bowland Shale is unlikely to be extensively developed as an unconventional hydrocarbon resource. Despite this, the Bowland Shale Formation remains an important conventional hydrocarbon source rock, for example in the North Sea (Monaghan *et al.* 2019). The Bowland Shale is a component of at least one geothermal play in the UK where it is a seal for interdigitating sandstone aquifers (Gluyas *et al.* 2018) and it caps

From: Emmings, J. F., Parnell, J., Stephenson, M. H. and Lodhia, B. H. (eds) 2024. *The Bowland Shale Formation, UK: Processes and Resources*. Geological Society, London, Special Publications, **534**, 61–90.
First published online March 22, 2024, https://doi.org/10.1144/SP534-2022-262

and buries several granitic intrusions in the UK (Leeder 1982; Busby and Terrington 2017), potentially enhancing this geothermal play. The Bowland Shale is a candidate source of base metals (Pb–Zn, Cu) (Parnell and Swainbank 1990; Kendrick *et al.* 2002; Juerges *et al.* 2016; Emmings *et al.* 2020*b*) and is a borderline highly enriched metalliferous black shale (Emmings *et al.* 2020*c*). Weathering of the Bowland Shale may release redox-sensitive metals and semi-metals into the environment, potentially impacting groundwater, soil quality and the health of livestock (Brogan *et al.* 1973; Parnell *et al.* 2016). The relatively high U content in the Bowland Shale (Emmings *et al.* 2020*c*) implicates it as a source of Rn, derived primarily from the decay of ^{238}U, which may contribute to the known Rn hazard in areas such as the Ribble Valley (Miles *et al.* 2007) or in deep groundwater aquifers. Finally, the Bowland Shale spans the mid-Carboniferous (Mississippian–Pennsylvanian) boundary and extinction event (Saunders and Ramsbottom 1986), representing a period of extreme climatic and oceanic conditions of interest to a range of deep time palaeoenvironmental and modern climate research questions (e.g. van de Velde *et al.* 2020).

Here we integrate sedimentological, geochemical and petrophysical observations through two cored sections of the Bowland Shale (historically recognized as the Holywell Shale in North Wales) in Ellesmere Port-1 to develop a high-resolution syngenetic and early diagenetic facies framework through the Bowland Shale. We utilize these observations to build on the idealized sea-level faunal/salinity and sedimentary stacking patterns recognized by Ramsbottom *et al.* (1962) and Holdsworth and Collinson (1988). Using machine learning of wireline data aligned to core scan X-ray fluorescence (XRF) data, we translate core-scale observations into predictions of sedimentological facies through the entirety of the Bowland Shale in Ellesmere Port-1, representing a *c.* 324 m thick succession spanning from the Arnsbergian (*c.* 329 Ma) to the Marsdenian or Yeadonian (*c.* 317 Ma). The facies framework and interpreted stacking patterns are relevant for any drilling activity into, or through, the Bowland Shale Formation. Finally, we provide new constraints on the radiogenic heat productivity (RHP) and heat flow through the Bowland Shale in Ellesmere Port-1. In an accompanying paper, Hennissen *et al.* (2024) explore the Bowland Shale in Ellesmere Port-1 in the context of hydrocarbon prospectivity.

Geological setting

Blacon Basin structure

Oblique collision between Gondwana and Laurussia during the Carboniferous (Warr 2000) prompted crustal back-arc extension across central and northern England and North Wales, within a seaway that extended from present-day North America to Poland (e.g. Davies *et al.* 1999). Extension generated a series of graben and half-graben separated by shelves and highs (Fig. 1), termed a 'block-and-basin' topography, aligned along inherited pre-Carboniferous structures and bounded by the Southern Uplands in the north and Wales–Brabant Massif (WBM) in the south (Leeder 1982; Fraser and Gawthorpe 1990, 2003; Waters and Davies 2006). This array of interconnected basins gradually merged owing to post-rift thermal subsidence through the Namurian, and are collectively defined as the Pennine Basin, representing a long-lived depocentre during most of the Carboniferous (Waters and Davies 2006).

Ellesmere Port-1 is situated on the NE margin of the Blacon Basin in North Wales and Cheshire, a sub-basin of the Pennine Basin (Andrews 2013), which was possibly linked to the Widnes Basin of Fraser *et al.* (1990) (Fig. 1). The Blacon Basin is bounded in the south by the Bryneglwys fault (the Bala Lineament) and WBM, in the west by the Nercwys–Nant-figillt Fault Zone, Vale of Clwyd Fault and North Wales Shelf, and in the NE by the Great Ewloe Fault, Edgerley–Waverton Fault Zone (EFZ) and ultimately the Central Lancashire High (Fig. 1) (Smith *et al.* 2005). The locus of deposition in the Blacon Basin was consistently centred immediately to the north of the Bala Lineament (on the downthrown hanging wall block), as evidenced by: (1) a thick Early Carboniferous carbonate succession (Smith *et al.* 2005); (2) thickening of Minera Formation (Brigantian) sandstones into the basin (Davies *et al.* 2004); (3) early Namurian (Pendleian) megasliding on the southwestern fringe of the basin (Kirkham 2021); (4) an expanded Namurian succession in the Blacon East-1 well in the Blacon Basin (Davies *et al.* 2004; Andrews 2013; Waters *et al.* 2021); (5) pinch-out of the Namurian succession on the margin of the North Wales Shelf in the west (Williams and Eaton 1993); and (6) a highly condensed Namurian succession in the Erbistock-1 well on the emergent landmass in the south (Andrews 2013) (Fig. 1). A condensed Namurian succession is also proven in the Milton Green-1 well (Andrews 2013) on the nearby Milton Green High (Smith *et al.* 2005).

During the Brigantian (regional substage in the latest Visean), widespread ramp-to-shelf carbonates of the Clwyd Limestone Group, including the Cefn Mawr Limestone Formation and Minera Formation, indicate development of shallow water carbonate platform and slope conditions (Somerville 1979; Davies *et al.* 2004, 2011; Waters *et al.* 2021). The Cefn Mawr Limestone Formation exhibits shoaling-upward sequences of wackestone, packstone and crinoidal limestone, often capped by karstic surfaces, soils and calcrete horizons. The

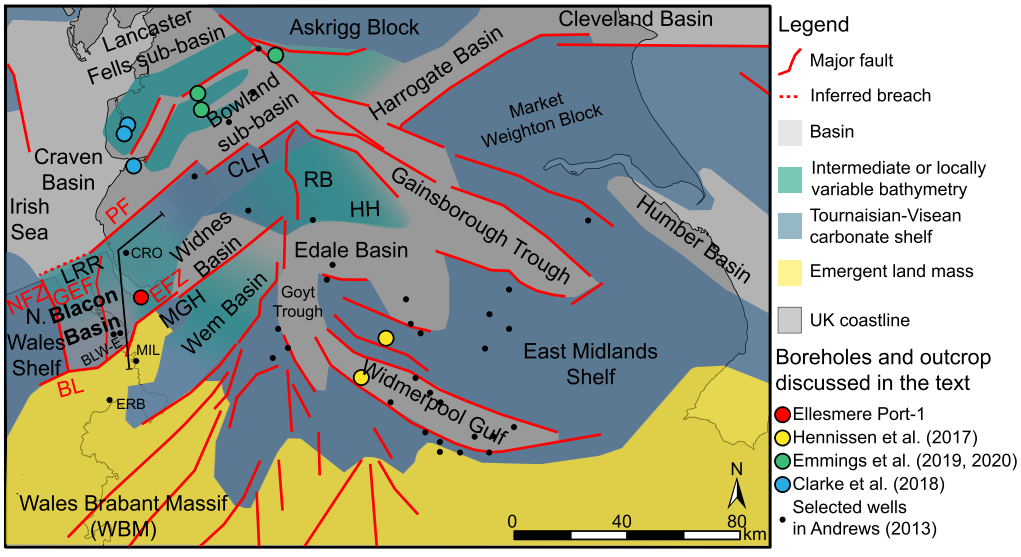

Fig. 1. Brigantian block-and-basin structures and key borehole and outcrop sections across central Britain, with emphasis on the vicinity of the Blacon Basin. BL, Bala Lineament; BLW-E, Blacon East-1 well; CLH, Central Lancashire High; CRO, Croxteth-1 well; EFZ, Edgerley–Waverton Fault Zone; ERB, Erbistock-1 well; GEF, Great Ewloe Fault; HH, Holme High; LRR, Llŷn–Rossendale Ridge; MGH, Milton Green High; MIL, Milton Green-1 well; NFZ, Nercwys–Nant-figillt Fault Zone; PF, Pendle fault; RB, Rossendale Basin. Source: after Andrews (2013), Fraser and Gawthorpe (1990, 2003), Fraser *et al.* (1990), Pharaoh *et al.* (2020), Smith *et al.* (2005), Waters and Davies (2006) and Waters *et al.* (2007, 2009, 2011, 2020, 2021).

sequences were primarily driven by eustatic sea-level fluctuation overprinted by late synrift tectonism, including subaerial platform exposure during lowstands (Somerville 1979). The Minera Formation, defined by cyclic sequences of mudstone, packstone, wackestone and calcareous sandstone, represents a fully subaqueous, proximal, sand-rich equivalent to the Cefn Mawr Limestone (Davies *et al.* 2004). Off-platform and distal to detrital sand input, the Brigantian succession grades laterally into the deep-water argillaceous carbonate slope apron facies of the Prestatyn Limestone Formation and the succeeding Teilia Formation (Warren *et al.* 1984; Davies *et al.* 2011). Initially shallow waters probably covered the Llŷn–Rossendale Ridge (Jackson *et al.* 1997; Smith *et al.* 2005). This high, representing the northern limit to the Blacon Basin, was probably connected to the Central Lancashire High (Fig. 1; *sensu.* Fraser and Gawthorpe 1990; DECC 2013) as the manifestation of the southwestern end of the Pendle fault system (Pharaoh *et al.* 2020). The presence of the Prestatyn Limestone and Teilia Formation near the NE margin the North Wales Shelf suggests that the Llŷn–Rossendale Ridge was a discontinuous feature, enabling weak connectivity between the Blacon Basin and distal Craven Basin (Davies *et al.* 2004; Waters *et al.* 2007; Andrews 2013; Juerges *et al.* 2016).

A transition from the Clwyd Limestone Group to the Craven Group at the Visean–Namurian boundary indicates an important regional shift from active rifting to thermal subsidence (Leeder 1982; Waters *et al.* 2009), and, as a consequence, a switch from a carbonate to siliciclastic depositional system (e.g. Fraser and Gawthorpe 2003). Cessation of active rifting and onset of thermal subsidence prompted progressive infill of the inherited Visean basin structures during the Namurian (Fig. 1). Assuming relatively sheltered conditions (Peters and Loss 2012), the inherited platforms and highs probably initially exhibited a water depth of less than 50 m. Taking the proximal Craven Basin as an analogue (Emmings *et al.* 2020*a*), the water depth in the Blacon Basin probably ranged from *c.* 100 to 200 m on the flanks and highs (Holdsworth and Collinson 1988; Davies 2008) to several hundred metres in the deepest part of the basin (Davies *et al.* 1993).

Namurian stratigraphy

The Pentre Chert Formation represents the basal part of the Craven Group in the Blacon Basin (Fig. 2), which unconformably overlies the Clwyd Limestone Group (Davies *et al.* 2004). The Pentre Chert is defined as a sponge spicule- and radiolarian-bearing chert deposited in relatively deep water, below storm

wave base (Davies *et al.* 2011). The Pentre Chert probably represents the condensed counterpart of Pendleian (E_1) siliceous mudstones of the Bowland Shale Formation in the Craven Basin (Emmings *et al.* 2020*a*, *b*). During the Pendleian, most of the siliciclastic sediment was sourced from the Pendle delta system in the north of the Craven Basin (Fraser and Gawthorpe 1990, 2003; Waters and Condon 2012), ensuring that the Blacon Basin remained isolated from detrital sediment. Deposition of siliceous sediments in the Blacon Basin during the Pendleian is consistent with: (1) development of widely hypoxic or intermittently anoxic bottom water conditions, favouring colonization by sponges (e.g. Schuster *et al.* 2021); (2) water column conditions that favoured colonization by radiolarians (Emmings *et al.* 2020*a*, *c*), perhaps associated with elevated riverine nutrient-loading and/or silica input (Dunham and Wilson 1985); and (3) increased influx of detrital mud onto platforms (potentially a distal extension of the Pendle delta), prompting regional termination of carbonate production (Davies *et al.* 2004).

The Pentre Chert is overlain by the Bowland Shale Formation (herein Bowland Shale), a highly heterogeneous, mudstone-dominated succession spanning from the mid-late Pendleian (*c.* 329 Ma) to Marsdenian or Yeadonian in Ellesmere Port-1 (*c.* 317 Ma; Fig. 2) (Davies *et al.* 2011; Waters and Condon 2012). The Bowland Shale definition adopted (Waters *et al.* 2009) encompasses the Holywell Shale in North Wales (e.g. Davies *et al.* 2004; Newport *et al.* 2016). The onset of third- to fourth-order sea-level fluctuation (Mitchum and Van Wagoner 1991; Waters and Condon 2012) coupled to thermal subsidence prompted deposition of the Bowland Shale across a wide range of basinal, prodelta and periodically emergent shelfal environments (Davies *et al.* 2004). The Pentre Chert and Bowland Shale grade laterally southwards into the Cefn-y-Fedw Sandstone Formation of the Millstone Grit Group derived primarily from the WBM (Fig. 2) (Davies *et al.* 2004; Waters *et al.* 2009, 2021). The Cefn-y-Fedw Sandstone comprises coarsening–upward cycles of quartzitic sandstones interbedded with subordinate mudstone and coal beds, interpreted as fluviodeltaic progradational sequences (Davies *et al.* 2004; Waters *et al.* 2021). In the Blacon Basin, three turbidite sand packages within the Bowland Shale represent the distal extensions of the Lower, Middle and Upper Cefn-y-Fedw Sandstone units (Davies *et al.* 2004; Waters *et al.* 2021). The Cefn-y-Fedw Sandstone is analogous and equivalent to sands of the Morridge Formation in the Widmerpool Gulf and Edale Gulf (Waters *et al.* 2009; Morton *et al.* 2015; Hennissen *et al.* 2017); both are associated with delta systems shed from the WBM in the south (Fraser and Gawthorpe 1990; Waters *et al.* 2021). The Bowland Shale grades into, and is overlain by, the fluviodeltaic Gwespyr Sandstone Formation (also Millstone Grit Group). Waters *et al.* (2021) showed that the Gwespyr Sandstone Formation derives from a combination of provenances from the south, north and west.

Marine bands. Marine transgressions and associated maximum flooding surfaces in the Bowland Shale are manifested as carbonate-rich, typically macrofauna-bearing sedimentary packages termed 'marine bands' (e.g. Ramsbottom 1977). Sea-level cyclicity in the Namurian was probably driven by far-field glaciation on Gondwana (Veevers and Powell 1987). The amplitude of sea-level fluctuation is estimated at 42 m (Maynard and Leeder 1992) or 60–100 m (Church and Gawthorpe 1994; Rygel *et al.* 2008). Marine bands on shelves mark the base of cyclothemic 'Yoredale' limestone–shale–sandstone triplets commonly capped by coal (e.g. Hampson 1997; Davies *et al.* 2004; Waters *et al.* 2007; Dean *et al.* 2011). Basinal marine bands are typically 1–5 m thick and are often overlain by an asymmetrical sequence of: (1) non-bioclastic, hemipelagic (lenticular) mudstone; and (2) turbidites, hybrid beds and debrites (Martinsen *et al.* 1995; Emmings *et al.* 2020*a*). Lowstands were associated with localized to extensive basinal sand deposition depending on proximity to delta systems (Millstone Grit Group). The third- and fourth-order marine band cycles may be superimposed onto 1.1–1.35 Myr duration Namurian 'mesothem' cycles (Ramsbottom 1979), associated with 17 major base-level falls (Waters and Condon 2012) and shifts in the loci of sediment deposition (Martinsen *et al.* 1995). Salinity fluctuations from fully marine (transgressions) to brackish or freshwater conditions are also widely recognized in the Bowland Shale on the basis of volumetric calculations (Holdsworth and Collinson 1988), macrofauna and microfauna such as conodonts (Ramsbottom *et al.* 1962; Holdsworth and Collinson 1988), biomarkers (Gross *et al.* 2015; Sims *et al.* 2024), sedimentology (Holdsworth and Collinson 1988; Gross *et al.* 2015; Emmings *et al.* 2020*a*, *c*) and inorganic geochemistry (Leeder *et al.* 1990; Maynard *et al.* 1991; Emmings *et al.* 2020*c*).

Coupled to sea-level and salinity fluctuation, palaeoredox proxies show that the Bowland Shale was deposited under fluctuating oxic, anoxic and at least intermittently sulfidic (euxinic) conditions (Leeder *et al.* 1990; Gross *et al.* 2015; Riley *et al.* 2018; Emmings *et al.* 2019, 2020*c*), a phenomenon probably driven by euhaline phytoplankton productivity. Euxinia in the Bowland Shale (and younger Carboniferous rocks) is most strongly associated with transgressions and maximum flooding, whereas reduced basin accommodation is linked to increased bottom water ventilation (Bloxam and Thomas 1968;

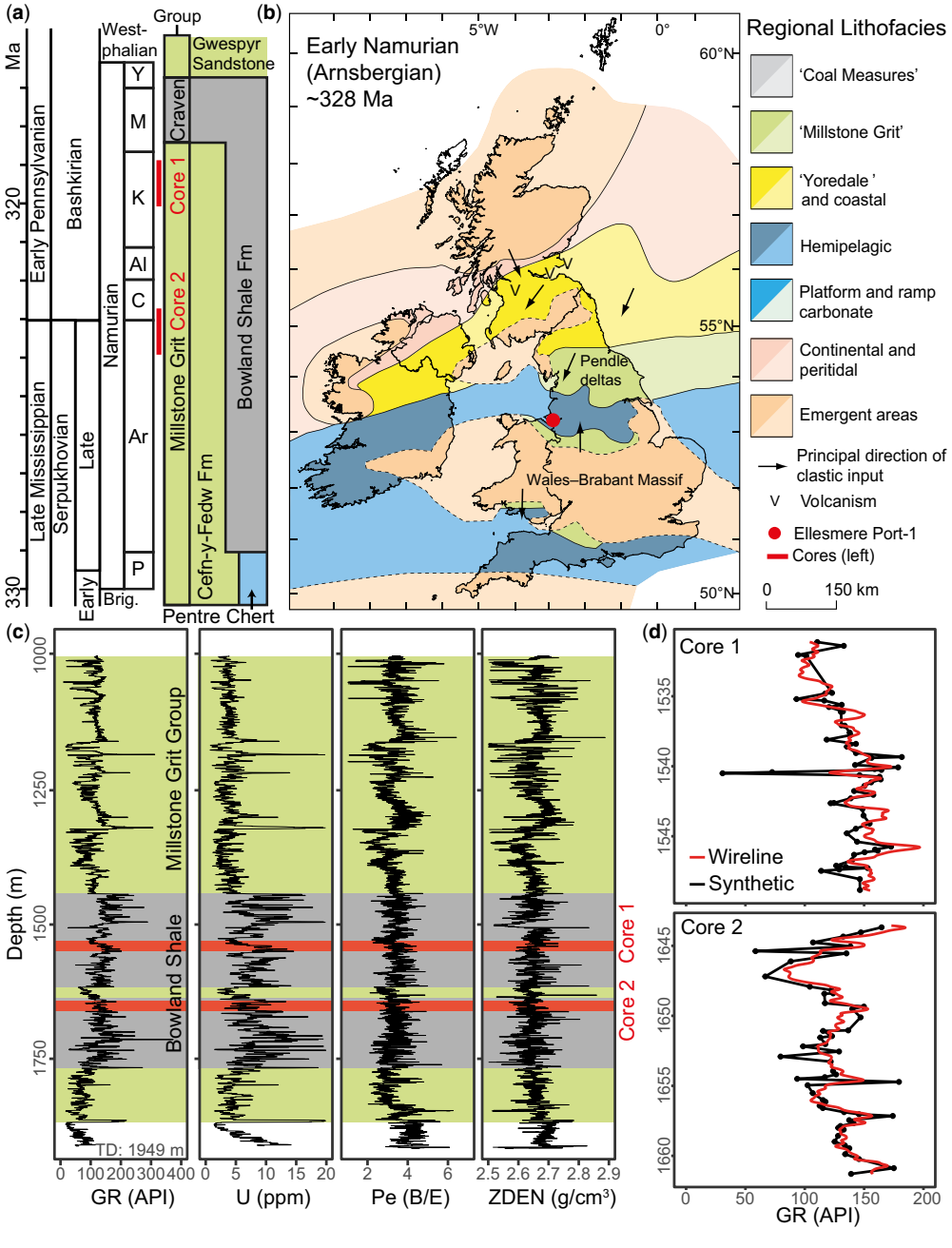

Fig. 2. General stratigraphy, regional Arnsbergian lithofacies and selected well log data. (**a**) Generalized stratigraphy and (**b**) regional lithofacies from Waters *et al.* (2007), including absolute ages (from Davydov *et al.* 2012; Waters and Condon 2012) and the updated Early–Late Serpukhovian boundary (Cózar and Somerville 2021). (**c**) The Bowland Shale Formation exhibits elevated total gamma-ray (GR, in American Petroleum Institute units (API)) and U (ppm) concentrations. (**d**) Correlation between wireline gamma v. synthetic gamma-ray (estimated from measured U, Th and K contents; see 'Methods') verifies the alignment of reported corebox depths to the wireline data (see Fig. 3). Ellesmere Port-1 is highlighted (53° 17′ 43.3841″ N, 02° 54′ 21.13091″ W; 339629 mE 378016 mN, British National Grid). Y, Yeadonian; M, Marsdenian; K, Kinderscoutian; Al, Alportian; C, Chokierian; Ar, Arnsbergian; P, Pendleian; Brig., Brigantian.

Leeder *et al.* 1990; Maynard *et al.* 1991; Fisher and Wignall 2001; Pearce *et al.* 2010; Gross *et al.* 2015; Emmings *et al.* 2020*c*). Considering the evidence for significant freshwater discharge from delta systems, shelfal anoxia (as opposed to basinal anoxia) was possibly caused by upwelling of marine anoxic bottom waters trapped beneath a freshwater lid (Algeo *et al.* 2008). By contrast trace-element quotas in the basinal shales favour the development of anoxia in weakly restricted, thermally stratified and highly productive water column conditions (Riley *et al.* 2018; Emmings *et al.* 2020*c*). Euxinia was potentially confined to mid-depth waters, potentially part of one or more linked regional-scale oxygen minimum zones that developed in the late Devonian (Kabanov and Jiang 2020; Emmings *et al.* 2022).

Macrofauna associated with the marine bands form the basis of a high-resolution biostratigraphic framework through the Namurian (Ramsbottom and Saunders 1985; Holdsworth and Collinson 1988). Marine bands and overlying mudstones exhibit the following idealized faunal sequence (phases 6 to 1): thick-shelled ammonoids (6); thin-shelled ammonoids (5); molluscan spat (4); *Lingula* (3); *Planolites* (2); fish remains (1); and barren zones (Ramsbottom *et al.* 1962; Baines 1977; Ramsbottom 1977). These faunal phases are thought to indicate cycling between euhaline (6) and freshwater conditions (1) (Ramsbottom *et al.* 1962; Holdsworth and Collinson 1988), although preservation or absence of bioclasts is also dependent on early diagenetic porewater conditions (Emmings *et al.* 2020*c*). The Bowland Shale in North Wales spans all the regional Namurian substages, from the Pendleian (E_1) to Yeadonian (G_1) (Davies *et al.* 2011). Marine bands exhibit an average periodicity of 111 kyr (Waters and Condon 2012), indicative of fourth-order cycles (Mitchum and Van Wagoner 1991). $E_{1c}1$, $E_{2a}2$, $E_{2b}3$, H_{1a}, $H_{2b}1$, R_{1b}, $R_{1c}4$, $R_{2a}1$, $R_{2b}1$, $R_{2c}1$, $G_{1a}1$ and $G_{1b}1$ peak flooding events are recognized in North Wales (Davies *et al.* 2011), probably related to third-order forcing (Mitchum and Van Wagoner 1991; Waters and Condon 2012). Multiple flooding surfaces are recognized for many of the marine bands, potentially linked to sub-100 kyr precession or obliquity cycles (Waters and Condon 2012).

Burial and uplift

Pb–Zn mineralization on the North Wales Shelf suggests thermal maturation and dewatering of adjacent basinal sediments in the latest Namurian (Juerges *et al.* 2016). During the late Pennsylvanian, closure of the Rheic–palaeo-Tethys seaway associated with the Variscan Orogeny (e.g. Leeder 1982) prompted a major depositional hiatus and the inversion of many basin structures across central England (e.g. Smith *et al.* 2005). In the Pennines, inversion combined with a relatively high basinal heat flow (in contrast to North Wales) enhanced basin dewatering and led to protracted Pb–Zn–F mineralization on blocks (Bouch *et al.* 2006; Hollis and Walkden 2012). Inverted structures in the vicinity of the Blacon Basin include the anticlines on the Bala Lineament and EFZ (Smith *et al.* 2005) and the Môn–Deemster–Ribblesdale fold belt in the north (Arthurton 1984; Pharaoh *et al.* 2020). The Cheshire Basin, partially superposed on the Blacon Basin, developed in response to renewed extension during the Permo-Triassic (Davies *et al.* 2004). The Permo-Triassic in the Cheshire Basin comprises aeolian and fluvial sediments (Sherwood Sandstone Group); Fe–Cu mineralization on the adjacent North Wales Platform may derive from charging by Permo-Triassic oxidized brines (Juerges *et al.* 2016) or from basinal Carboniferous fluids (Parnell and Swainbank 1990). Maximum burial of the Blacon Basin was probably attained in the Late Cretaceous, prior to Tertiary uplift (Williams and Eaton 1993; Green *et al.* 1997; Pharaoh *et al.* 2019).

Materials and methods

Logging and sampling

Two 17.8 m cored sections through the borehole Ellesmere Port-1 (53° 17′ 43.3841″ N, 02° 54′ 21.13091″ W; 339629 mE 378016 mN, British National Grid), drilled by IGas Energy in 2014, were logged and sampled at the National Geoscience Data Centre (NGDC) core repository, British Geological Survey. Sedimentological structures and facies were logged prior to major- and minor-element XRF core scanning and sampling. The reported absolute core depths were aligned with the reported wireline absolute depth by matching features observed in core to the borehole image logs (Figs 2 & 3). For validation, we compared synthetic (derived from discrete XRF) and measured gamma-ray curves (Fig. 2). The wireline gamma ray tends to smooth across thin beds exhibiting particularly high or low true (synthetic) gamma-ray values, but overall, the synthetic and wireline gamma-ray datasets are strongly correlated (Fig. 2d). This assessment indicated an offset of 1.6 and 1.76 m between the downhole absolute depth and reported cored depth, for core 1 and core 2, respectively. The synthetic total gamma ray was estimated from bulk U, Th and K concentrations using the approximation of Ellis and Singer (2007) (equation 1):

$$\mathrm{GR(API)} = 4\mathrm{Th} + 8\mathrm{U} + 16\mathrm{K} \qquad (1)$$

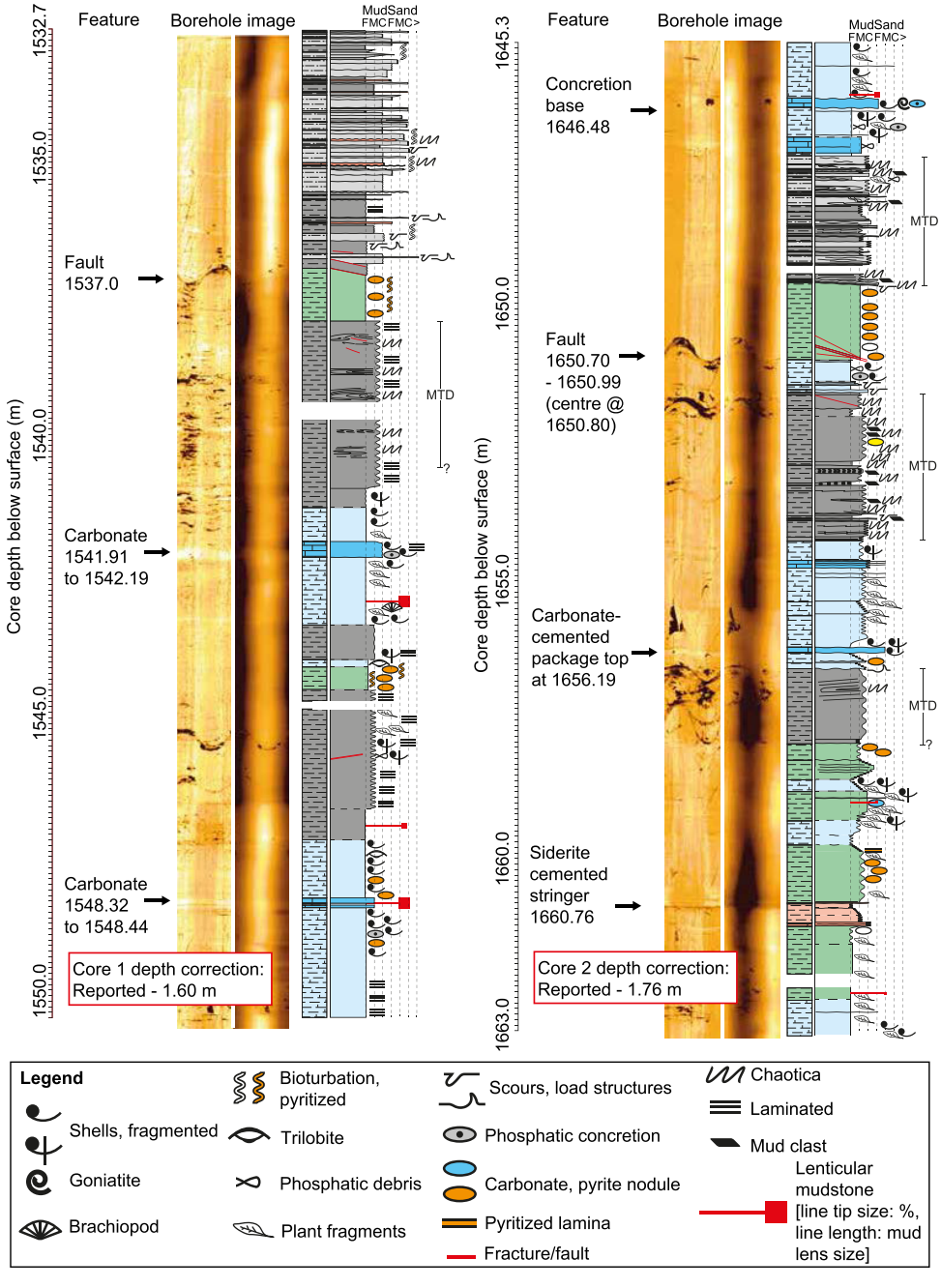

Fig. 3. Key static borehole image log and core observations used for the alignment of reported well and core depth. Depth alignment was achieved by matching the same linear features present in both datasets. MTD, mass transport deposit.

Core scan XRF measurements were collected using an Itrax MC core scanner (Cox Analytical Systems) in the Core Scanning Facility at the British Geological Survey, Keyworth. This dataset is available under Open Government Licence (BGS Core Scanning Facility 2022). Before core scanning, fragments of the split core were aligned with a levelling tool to ensure optimal alignment of the detector.

XRF was measured at a 1 cm step-size and 30 s integration time. For each core section, an initial surface scan was performed to compute the trajectory of the XRF detector. The Itrax MC core scanner automatically produces an XRF sum spectrum for each core section, which was peak-fitted using the processing software Q-Spec version 8.6 (Cox Analytical Systems, Sweden). A single fitting template was used to fit most of the core data. Core horizons that showed high Ca, Fe or Cl elemental abundances were refitted accordingly. These fitted XRF data were exported as elemental peak areas (counts) for processing in R. Data were aggregated into the two core runs and assigned a true core depth. The dataset was cleaned to remove erroneous data points, for example spanning cracks, missing core sections and intervals of generally poor core quality.

Bulk geochemistry

A total of 110 samples, split between core 1 (57 samples) and core 2 (53 samples), were selected for bulk major- and trace-element geochemistry, Rock-Eval pyrolysis, palynology (see Hennissen *et al.* 2024) and stable isotope analysis. Discrete XRF major- and trace-element data were acquired on fused beads (using ignited sample powders) and powder briquettes at the University of Leicester, using a PANalytical Axios Advanced XRF spectrometer and default PANalytical SuperQ conditions (Malvern PANalytical, Malvern, UK). Repeat analyses of reference materials and prior Bowland Shale samples indicate an XRF accuracy of $\pm 5\%$ for major elements and $\pm 5\%$ for trace elements, and a precision of up to $\pm 5\%$ (but commonly $\pm 1\%$, 2σ) for major elements and $\pm 10\%$ (but commonly $\pm 5\%$) for trace elements (Emmings 2018; Emmings *et al.* 2020*c*).

Total sulfur (TS) content was determined via a Flash 1112 elemental analyser coupled to an isotope ratio mass spectrometer at the National Environmental Isotope Facility (NEIF) laboratory at the British Geological Survey. TS accuracy and precision are estimated at $\pm 15\%$ and ± 0.2 wt% S, respectively, based on repeat analyses and independent measurement via LECO elemental analysis (Emmings *et al.* 2020*c*). Trace-element enrichment factors (EFs; e.g. Tribovillard *et al.* 2006) were utilized using Post–Archean Average Shale (PAAS) (Taylor and McLennan 1985) (equation 2) and local mean concentrations (*sensu* Emmings *et al.* 2020*c*). Pyrolysis was conducted in standard mode using a Rock-Eval 6 apparatus (Vinci Technologies, Nanterre, France) at the British Geological Survey. Accuracy is typically 1–2% for most Rock-Eval parameters, based on repeat analyses of the IFP Rock-Eval standard. Repeat analyses of similar Bowland Shale samples indicate a precision (2σ) of ± 0.11 mgHC g^{-1} (S1), ± 0.44 mgHC g^{-1} (S2) and ± 0.03 wt% total organic and inorganic carbon (total organic carbon; TOC, inorganic/mineral carbon; MINC). Derived Rock-Eval parameters include the oil saturation index (OSI) and hydrogen index (HI) (Lafargue *et al.* 1998).

$$\mathrm{EF_{element}} = (X/\mathrm{Al})_{\mathrm{sample}}/(X/\mathrm{Al})_{\mathrm{PAAS}} \qquad (2)$$

The original TOC (TOC_o) was calculated for palynological samples using the method of Jarvie (2012*a*) and values are reported in Hennissen *et al.* (2024). TOC_o was extrapolated for all discrete samples ($n = 110$) via a linear regression between the calculated TOC_o and present-day TOC (TOC_{pd}, $r^2 = 0.99$; see Supplementary material; equation 3), where:

$$\mathrm{TOC_o} = 1.16\,\mathrm{TOC_{pd}} - 0.16 \qquad (3)$$

On the basis that the core sections are oil to marginally gas-mature (Hennissen *et al.* 2024), TOC_o was preferred over TOC_{pd} for a more robust S/TOC palaeosalinity proxy (Raiswell and Berner 1987).

Stable isotopes. All stable isotope data are reported in standard delta (δ) notation as per mil (‰) variations. Bulk S isotope ratios were measured using a Thermo Fisher Delta Plus XL isotope ratio mass spectrometer interfaced with a Flash 1112 elemental analyser. $\delta^{34}S_{bulk}$ values are reported on the Vienna-Canyon Diablo Troilite standard (VCDT) scale. S isotope ratios were calibrated using a linear fit through IAEA-S-1 (−0.3‰), IAEA-S-2 (+22.67‰) and IAEA-S-3 (−32.3‰). $\delta^{34}S_{bulk}$ reproducibility is ± 1.2‰ (2σ) based on repeat analyses.

Bulk C isotope analyses were performed by combustion in a Costech ECS4010 Elemental Analyser on-line to a VG TripleTrap and Optima dual-inlet mass spectrometer, with $\delta^{13}C$ values calculated to the Vienna Peedee Belemnite (VPDB) scale using within-run laboratory standards calibrated against the NBS-19 and NBS-22 (VPDB) scale, using within-run laboratory standards (NBS19 +1.95‰ and NBS22 −30.03‰). $\delta^{13}C_{org}$ reproducibility is $\pm <0.1$‰ (1σ). C/N ratios are calibrated against a Broccoli standard (BROC2). Replicate analysis of well-mixed samples indicated a precision of $\pm <0.1$‰.

Data manipulation and analysis

All data manipulation and statistical analysis was coded in R using RStudio (R Core Team 2018). XRF core scan, discrete analyses (conventional XRF, stable isotopes, Rock-Eval pyrolysis) and wireline data were manipulated using the following R packages: ggplot2 (Wickham 2009), gridExtra

(Auguie 2016), zoo (Zeileis and Grothendieck 2005), plyr and dplyr (Wickham and Francois 2016), data.table (Dowle and Srinivasan 2020), compositions (van den Boogaart *et al.* 2020), ggtern (Hamilton 2017) and caret (Kuhn 2020). Chemofacies were determined by hierarchical cluster analysis (HCA) of principal component analysis (PCA) scores (e.g. Emmings *et al.* 2022) using selected core scan XRF major and minor elements (Mg, Al, Si, P, K, Ca, V, Mn, Fe, Ni, As, Sr, Zr, Mo and Ba). These elements were selected on the basis of relatively high abundances, and as proxies for detrital phases (Al, Si, K, Zr; e.g. Hild and Brumsack 1998; Emmings *et al.* 2020*a*), Fe oxides (Fe, As; e.g. Tribovillard 2020), autochthonous input including biogenic and diagenetic carbonates (Si, Ca, Mn, Mg, Sr, Ba, P) and palaeoredox (Fe, Mn, Mo, V, Ni, As; e.g. Tribovillard *et al.* 2006). Processed count data were not converted to absolute concentrations; this approach circumvents closed data effects that require transformation prior to statistical analysis (e.g. centred log-ratio; Aitchison 1986). PCA was conducted on the correlation matrix (scaled and centred data). The first six principal components were selected on the basis of assessment of the hinge point on the scree plot. HCA of the sample scores for the first six principal components was conducted via the sum of squares (Ward clustering) and Euclidian distance matrix.

Machine learning. We explored the potential of machine learning to aid in extrapolating the core scan clusters (e.g. chemofacies) through the Bowland Shale Formation. Ahead of machine learning, the seven chemofacies were aggregated into four classes: limestones (A); weakly to moderately calcareous mudstones and siltstones (C–E); claystone density flow deposits (B, F); and siltstone to sandstone density flow deposits (G). Simplification into four classes for machine learning was justified on the basis of (1) experimentation to optimize the balance between the accuracy and complexity of predictions and (2) the thickness of beds and co-occurrences with other chemofacies: specifically, laminae of siderite-cemented claystone or siltstone are not directly resolvable in the well log data, but commonly co-occur with the claystone chemofacies (F).

The *k*-nearest neighbour (kNN) algorithm was selected for machine learning based on superior accuracy compared to linear discriminant analysis (LDA), classification and regression trees (CART), support vector machine (SVM) and random forest methods. The four simplified chemofacies classes were matched to the nearest, depth-aligned well log datum. The models were trained and deployed using the following well log data: compensated neutron porosity (CN); compressional wave slowness (DTC); shear wave slowness (DTS); spectral gamma-ray (U, Th, K); photo-electric (PE); and calculated formation bulk density (ZDEN). We trialled three approaches: (1) kNN using raw wireline data (87% accuracy at 0.05 *P*-value, optimal k = 7); (2) kNN using standardized (scaled and centred z-score) wireline data (89% accuracy at 0.05 *P*-value, optimal k = 5); and (3) kNN using standardized data and with null well log values (−9999) removed (87% accuracy at 0.05 *P*-value, optimal k = 5). Training, verification and accuracy estimation was determined on a 4:1 training-to-verification split. It is beyond the scope of this chapter to further refine the machine learning algorithms, but future work could impute null values (e.g. Dmitrijeva *et al.* 2020) as a compromise between methods (2) and (3). The trained models were deployed on the entire Bowland Shale section at Ellesmere Port-1 (1443 to 1767 m below surface) to delineate limestone, calcareous mudstone, claystone and siltstone to sandstone (density flow).

RHP and heat flow

RHP (in $\mu W\ m^{-3}$) was calculated using the equation of Rybach (1976) (equation 4):

$$\mathrm{RHP} = (1000p)(10^{-5})[(9.52\,\mathrm{U}) + (2.56\,\mathrm{Th}) + (3.48\,\mathrm{K})] \quad (4)$$

where U, Th and K concentrations are in ppm, ppm and wt%, respectively, and p is the bulk density ($g\ cm^{-3}$). We assume $p = 2.6\ g\ cm^{-3}$ for the Bowland Shale (Clarke *et al.* 2018). The temperature gradient through the Bowland Shale was modelled using the equation of Beardsmore *et al.* (2010), where T is the temperature at the base of the given sedimentary package, T_0 is the temperature at the top of the package, Q_0 is the surface heat flow ($W\ m^{-2}$), K_s is the thermal conductivity ($W\ m^{-1}\ K^{-1}$), A_s is RHP (in $W\ m^{-3}$) and S is the thickness of the sedimentary package (m), and inversely proportional to the thermal conductivity (K_s in $W\ m^{-1}\ K^{-1}$), as defined by equation (5):

$$T[^{\circ}\mathrm{C}] = T_0 + [(Q_0 x\ S)/K_s] - (A_s)[S^2/(2K_s)] \quad (5)$$

Results and discussion

Syngenetic processes

Based on macrofaunal (ammonoid) biostratigraphy, cores 1 and 2 are assigned to the Late Kinderscoutian (R_1c1) and late Arnsbergian–Chokierian ($H_{1a}1$–$H_{1a}3$) biozones, respectively (Figs 4 & 5). Thus, core 2 spans the onset of the mid-Carboniferous boundary (Saunders and Ramsbottom 1986), although the presence of intervening faults and a paucity of diagnostic Arnsbergian macrofauna does

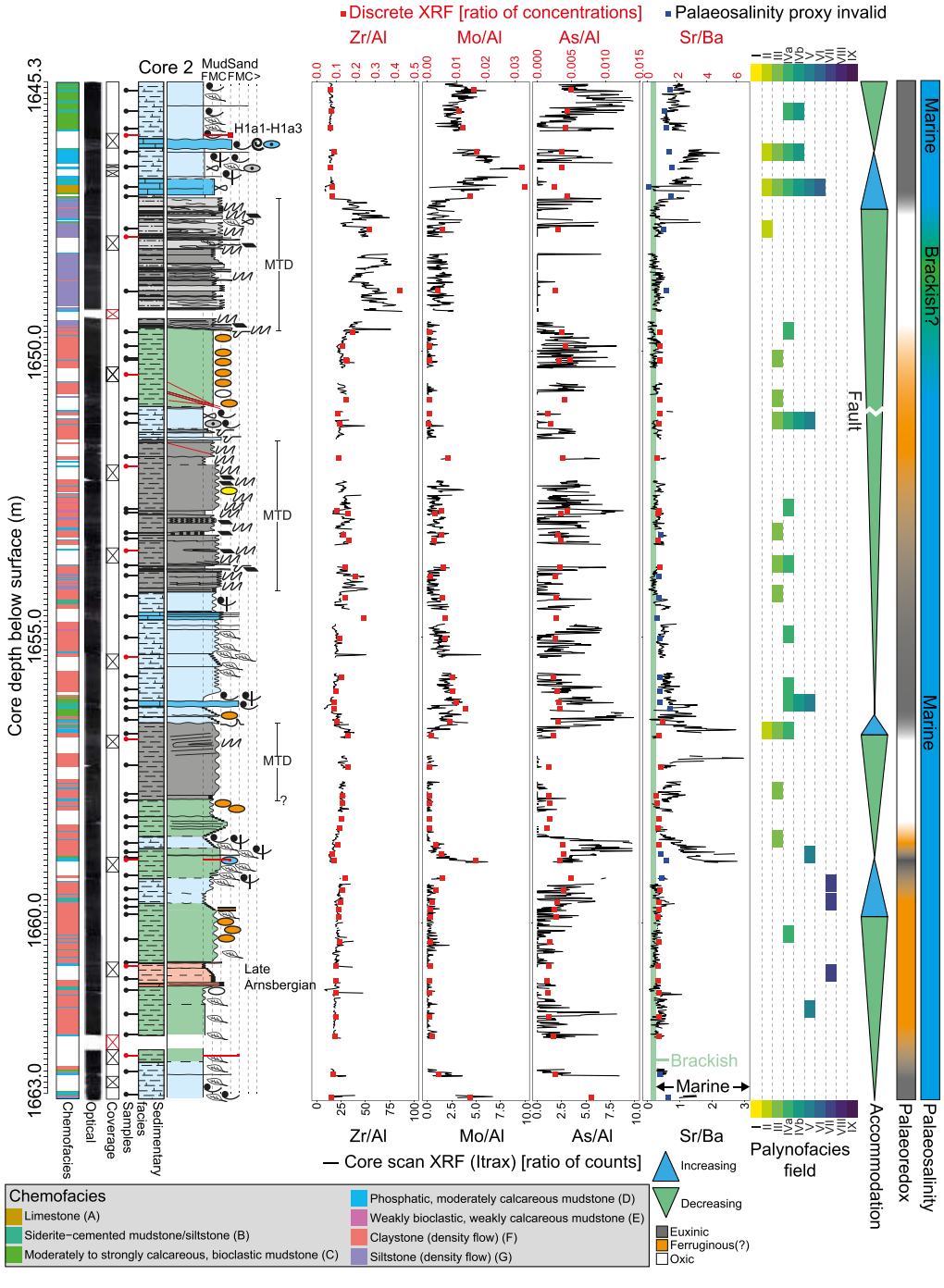

Fig. 4. Sedimentology and selected geochemistry through the late Arnsbergian–Chokierian Bowland Shale in Ellesmere Port-1 (core 2). See Figure 3 for key to sedimentary structures. Palynofacies data are from Hennissen *et al.* (2024), using the fields of Tyson (1995). I, highly proximal shelf/basin; II, marginal dysoxic–anoxic basin; III, heterolithic (proximal) shelf; IVa, dysoxic–suboxic shelf edge; IVb, dysoxic–anoxic shelf edge; V, mud-dominated (distal) oxic shelf; VI, proximal suboxic–anoxic shelf; VII, distal dysoxic–suboxic shelf; VIII, distal dysoxic–anoxic shelf; IX, distal suboxic–anoxic basin. MTD, mass transport deposit.

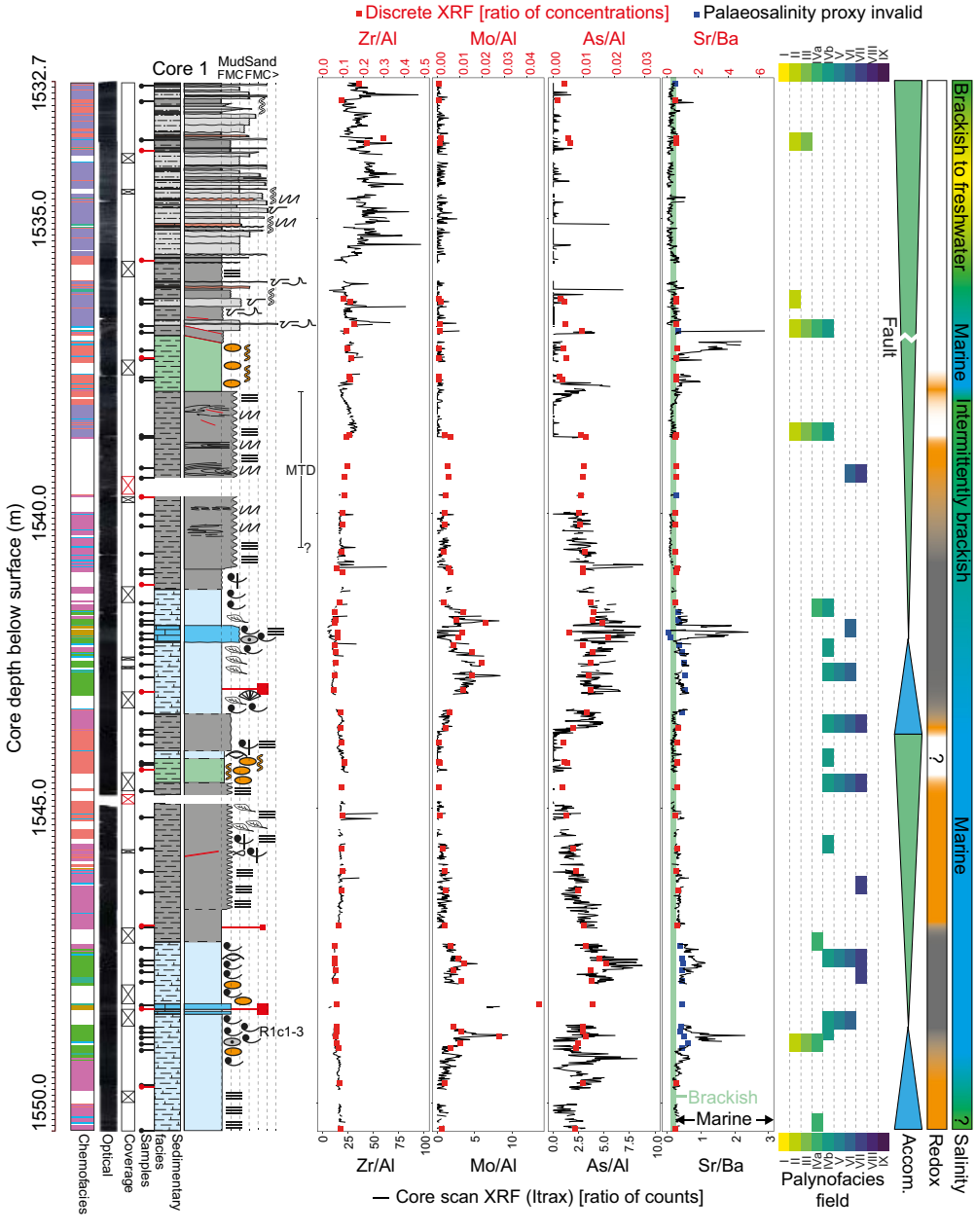

Fig. 5. Sedimentology and selected geochemistry through the late Kinderscoutian Bowland Shale in Ellesmere Port-1 (core 1). See Figure 3 for key to sedimentary structures. Palynofacies data are from Hennissen *et al.* (2024), using the fields of Tyson (1995). I, highly proximal shelf/basin; II, marginal dysoxic–anoxic basin; III, heterolithic (proximal) shelf; Iva, dysoxic–suboxic shelf edge; IVb, dysoxic–anoxic shelf edge; V, mud-dominated (distal) oxic shelf; VI, proximal suboxic–anoxic shelf; VII, distal dysoxic–suboxic shelf; VIII, distal dysoxic–anoxic shelf; IX, distal suboxic–anoxic basin. MTD, mass transport deposit.

not preclude the potential for hiatuses beneath the $H_{1a}1$–$H_{1a}3$ interval. The core sections comprise packages of (1) massive, weakly to strongly calcareous, non-bioclastic to bioclastic mudstones, often interbedded with thin limestone beds, overlain by (2) thinly laminated or chaotic, non-calcareous

claystone beds (Figs 4 & 5). The calcareous, bioclastic mudstones are often macrofauna-bearing and are collectively interpreted as basinal marine band facies, characteristic of the Bowland Shale, deposited during fourth-order marine transgressions and highstands (e.g. Martinsen *et al.* 1995; Waters and Condon 2012).

The overlying non-calcareous claystone packages represent deposition from a range of turbulent, hybrid and laminar flows (e.g. Talling *et al.* 2012) during falling basin accommodation (Figs 4 & 5). In some cases the non-calcareous claystone packages contain pyritized organic matter and pyrite nodules, similar to the Bowland Shale in the Craven Basin, suggestive of intermittently non-steady-state sulfidic pore water conditions (Emmings *et al.* 2020*c*). In many cases, consecutive, stacked chaotica suggest that the claystone packages were transported en masse, potentially as discrete, metre-scale blocks rafted within debris flows (e.g. mass transport deposits; MTDs). Towards to the top of both core sections, the non-calcareous claystones are capped by thinly to thickly laminated, interbedded, bioturbated siltstone and sandstone facies, probably deposited during lowstands. In core 1, the contact between the siltstones and the underlying claystones is faulted; thus, the sequence stratigraphic relationship is unclear.

Zr/Al aliases the heavy mineral (zircon) component and is interpreted as a local proxy for the detrital grain size in this system (e.g. silt- to sand-fraction; Dowey and Taylor 2020; Emmings *et al.* 2020*a*). This is consistent with the observed relationship between Zr/Al and sedimentary facies; the marine band, claystone and siltstone facies exhibit low, medium and high to very high Zr/Al, respectively (Figs 4 & 5). Mo is a redox-sensitive metal that is fixed under at least intermittently sulfidic pore water conditions (e.g. Tribovillard *et al.* 2006). Elevated Mo/Al within the marine band packages (in both core sections) suggests the development of anoxic and intermittently sulfidic conditions coupled to sea-level rise. This is consistent with a productivity-driven, weakly restricted model for anoxia during deposition of the Bowland Shale (Emmings *et al.* 2020*c*). Arsenic is also redox-sensitive in the marine environment, but interpretation in terms of palaeoredox is generally complex (Tribovillard 2020). In this system, As/Al tends to co-vary with Mo/Al (Figs 4 & 5); this suggests operation of a strong Fe–Mn (oxyhydr)oxide shuttle during deposition (Tribovillard 2020), analogous to the model for anoxia in the adjacent Craven Basin (Emmings *et al.* 2020*c*). As/Al enrichment tends to span a wider depth interval compared to Mo/Al, and As/Al sinuosity, particularly in core 1, suggests generally high sensitivity to intermediate redox conditions compared with Mo/Al. Thus, high As/Al coupled to low Mo/Al is interpreted to indicate ferruginous water column conditions overlying non-sulfidic pore waters (Figs 4 & 5).

Finally, the palaeosalinity measure Sr/Ba (Wei and Algeo 2020) shows that conditions were generally marine and intermittently brackish. Whilst the Sr/Ba salinity proxy is limited to non-carbonate-bearing lithologies, the presence of euhaline macrofauna within the marine band facies permits a comprehensive reconstruction of the palaeosalinity variation throughout both cores (Figs 4 & 5). Several of the interpreted falling stage to lowstand sedimentary packages exhibit Sr/Ba <0.5; this suggests deposition under at least intermittently brackish conditions during periods of reduced basin accommodation. Sr/Ba shows that reduced salinity was more prevalent in the late Kinderscoutian section (core 1) compared to the generally more saline Arnsbergian–Chokierian section (core 2); this is consistent with the increasing proximity (i.e. progradation) of the Cefn-y-Fedw delta system towards the top of the Bowland Shale.

Cluster analysis of selected XRF core scan major and minor elements delineates seven chemofacies (A–G), interpreted as: limestone deposited under sulfidic conditions (A); siderite-cemented claystone or siltstone deposited under mixed redox conditions (B); bioclastic, moderately to strongly calcareous mudstone deposited under sulfidic conditions (C); weakly to moderately calcareous phosphatic mudstone deposited under mixed redox conditions (D); weakly bioclastic, weakly calcareous mudstone deposited under weakly sulfidic to non-sulfidic conditions (E); claystone deposited under oxic or suboxic conditions (density flows) (F); and siltstone to sandstone deposited under oxic or suboxic conditions (density flows) (G). Thus, the chemofacies are an objective measure for lithological variation, supplementary to the conventional sedimentological descriptions (Figs 4 & 5). The XRF core scan chemofacies are generally consistent with the conventional sedimentary descriptions, although there are some discrepancies, particularly in the assignment of calcareous and non-calcareous sediments. This is best explained by the difficulty in the visual estimation of the fraction of carbonate (e.g. reaction with a small amount of HCl).

A pseudo-compositional ternary plot of the core scan XRF data indicates most intervals are argillaceous, and less commonly quartz or carbonate-rich (Fig. 6). Carbonate-bearing, siliceous mudstones are rare (Fig. 6); this is consistent with the absence of silica cementation in the two cored sections. The discrete quantitative XRF analyses support this observation; dual Si v. Al (Fig. 7a) and Si v. Zr (Fig. 7b) biplots of Emmings *et al.* (2020*b*) show that biogenic silica is negligible in the two cored intervals. Thus, it is clear the cored sections are not

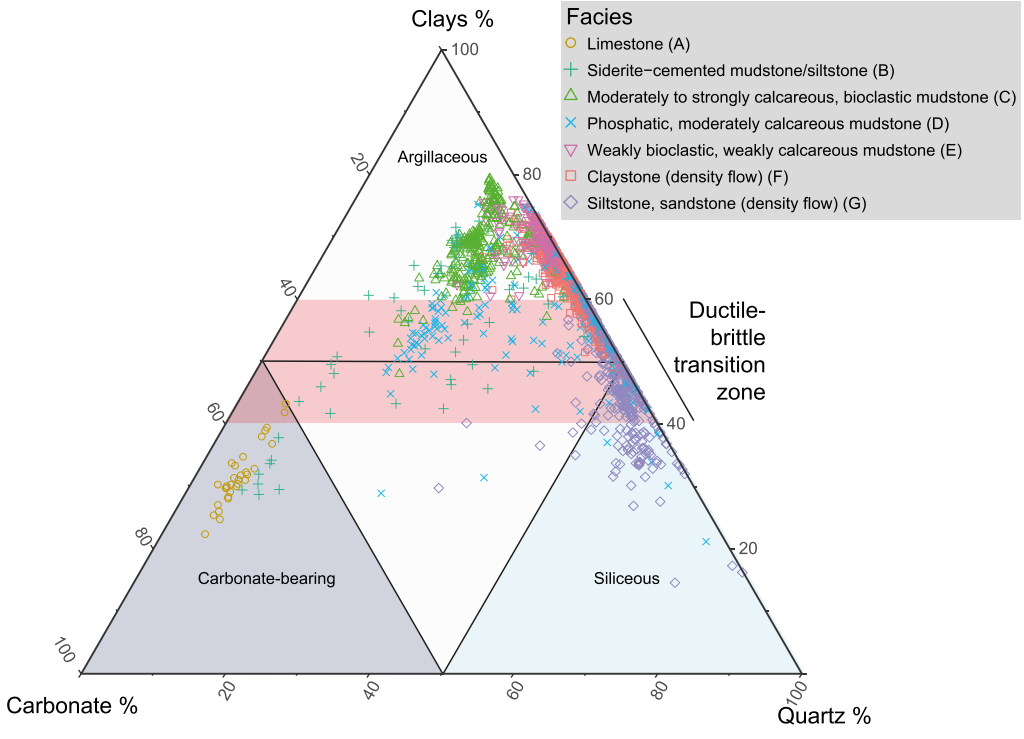

Fig. 6. Clay, carbonate and quartz bulk compositional ternary plot estimated using scaled core scan XRF count data (2Al, 0.05Ca and 10Zr, respectively). See text for discussion.

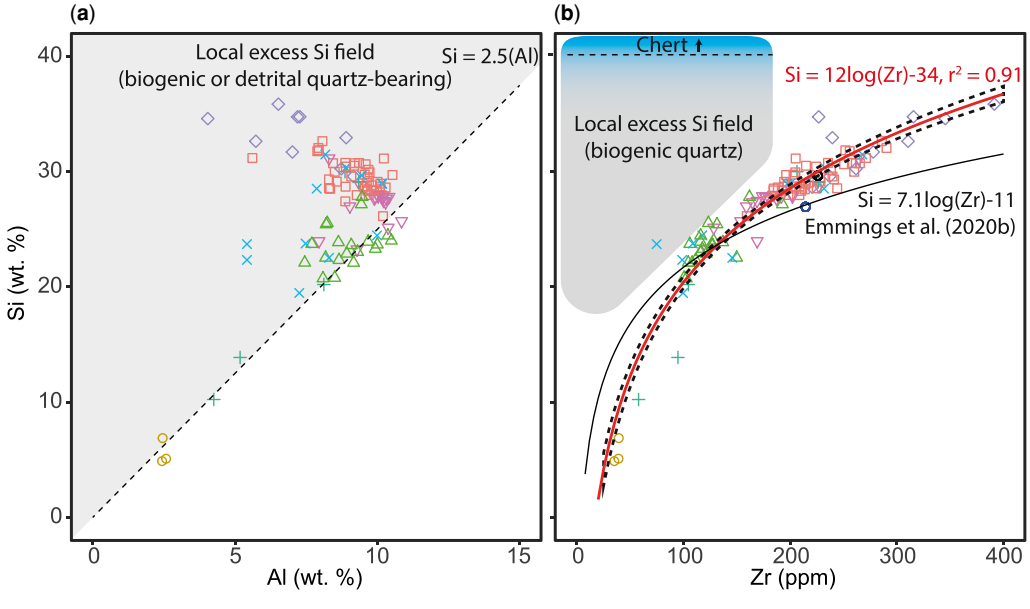

Fig. 7. Excess silica biplots, after Emmings *et al.* (2020*b*). Regression lines for the Ellesmere Port-1 data (red line, with 95% confidence interval) and Emmings *et al.* (2020*b*) are also plotted. The excess Si field delineates siliceous mudstones. The field is calibrated for Bowland Shale mudstones and compositionally immature siltstones and is not necessarily valid for other sedimentary rocks. See Figure 6 for key to facies.

comparable to, or transitional from, the underlying Pentre Chert and do not contain reworked biogenic silica. By extension, the lack of pervasive cementation shows that the cored sections in Ellesmere Port-1 are not comparable to key intervals in the Craven Basin, such as: (1) the siliceous mudstones of the Upper Bowland Shale (Emmings *et al.* 2020*b*); and (2) the calcareous and siliceous mudstones and limestones of the Lower Bowland Shale (e.g. Fauchille *et al.* 2017, 2018; Newport *et al.* 2018). Instead, the observed pattern of interfingering argillaceous and carbonate marine band facies is more comparable to the Bowland Shale in other paralic basins, such as the Widmerpool Gulf (Könitzer *et al.* 2014; Hennissen *et al.* 2017).

Each discrete sample spans *c.* 2 cm stratigraphic thickness. Taking a local mean sediment accumulation rate (mSAR) of *c.* 22 mm kyr^{-1} (Emmings *et al.* 2020*b*, after Davies *et al.* 2004) and 55% compaction (Emmings *et al.* 2020*a*), each sample represents a *c.* 2 kyr duration. This is a first-order estimate since the compaction ratio and mSAR are dependent on sedimentary facies (e.g. Shanmugam and Moiola 1982; Droxler and Schlager 1985; Emmings *et al.* 2020*a*). Enrichment factors for discrete XRF analyses support the interpretations based on the core scan XRF dataset. The strongly to weakly carbonate-bearing chemofacies (A–E) are consistently enriched in a suite of redox-sensitive elements, including Se, Mo, U, Zn, V, Ni and Fe (Fig. 8). Se enrichment is a prominent and unusual characteristic of the Bowland Shale that is best explained by ashfall inputs from far-field active volcanic centres (e.g. Brandon *et al.* 1995; Spears *et al.* 1999) or derived from weathering of volcanic rocks in the hinterland, followed by trapping under sulfidic conditions (Parnell *et al.* 2016). Parnell *et al.* (2022) show that Se, Mo and, to a lesser degree, As are complexed with organic matter and contained within pyrite in the Bowland Shale. By contrast Cu and U, other important redox-sensitive elements, are primarily hosted within recalcitrant (e.g. silicate or refractory kerogen) phases.

Chemofacies A limestones are fine grained, lack bioclasts and exhibit high concentrations of elements that proxy for carbonate, including Ca, Mg and Ba (Fig. 8). The limestone beds also lack internal sedimentary structures, suggestive of an early diagenetic origin (e.g. spherulitic limestones; Emmings *et al.* 2020*c*). Enrichment in redox-sensitive elements suggests early diagenetic precipitation via anaerobic oxidation of methane (Mazzini *et al.* 2004), similar to Pendleian spherulitic limestones observed in the Craven Basin (Emmings *et al.* 2020*a*). Siderite-cemented beds (chemofacies B) are most commonly interbedded with the claystone facies and exhibit relatively high concentrations of Mg, Fe and Mn, and moderate Ca (Fig. 8), consistent with dolomite and/or siderite cementation. The marine band packages are dominated by bioclastic calcareous mudstones (chemofacies C and D), interpreted as hemipelagic muds interbedded with subordinate calci-turbidites. The phosphatic chemofacies D is rare in core 1 and more common in core 2, consistent with phosphate input or fixation associated with generally more marine and productive conditions during the Arnsbergian (e.g. fish debris, authigenic phosphate). The marine band packages are typically overlain by chemofacies E, F and/or G, interpreted as falling sea-level and/or lowstand deposits.

The low $\delta^{34}S_{bulk}$ and large offset from $\delta^{34}S$ of contemporaneous seawater sulfate of *c.* 13–15‰ (Kampschulte *et al.* 2001; Kampschulte and Strauss 2004) in chemofacies A–E suggests precipitation of solid sulfides under open system conditions (e.g. Mossmann *et al.* 1991). In contrast, chemofacies F and G lack enrichment in redox-sensitive elements and exhibit variable, relatively high $\delta^{34}S_{bulk}$ (Fig. 8). High $\delta^{34}S_{bulk}$ in chemofacies F and G is best explained by precipitation of pyrite under closed system (i.e. relatively late diagenetic) conditions and/or quantitative sulfate. Any sulfate in chemofacies F and G is likely to be finely disseminated in the sedimentary matrix. Leached zones along the margins of the conjugate faults at *c.* 1537.73 m in core 1 (Fig. 5) exhibit $\delta^{34}S_{bulk}$ of +19.8 to +22.6‰; this is best explained by the presence of secondary sulfate that precipitated during the passage of late diagenetic oxidizing fluids.

Mississippian terrestrial OM typically exhibits −23.9‰ (Peters-Kottig *et al.* 2006) to −25.1‰ $\delta^{13}C_{org}$ (Könitzer *et al.* 2016), whereas amorphous organic matter (AOM; of probable marine origin) is usually close to *c.* −29.1‰ (Lewan 1986). $\delta^{13}C_{org}$ exhibits a consistent range between– 27‰ and– 24‰ in all sedimentary facies (Fig. 8), favouring a generally mixed to terrestrial origin for the organic matter (see Hennissen *et al.* 2024 for further discussion). The C/N ratio is relatively wide ranging (C/N 5–25). The marine, hemipelagic, anoxic chemofacies (A–D) have higher C/N than the oxic, density flow chemofacies (F–G). Considering C/N as a proxy for organic matter type, the C/N ratios are counter-intuitive because cellulose, abundant in C_3 and C_4 land plants, is N-deficient. Thus, fresh land plant material typically has a C/N >20 whereas marine algal and bacterial sources have a C/N <10 (Meyers 1994). Yet the reverse is observed in the two core sections: chemofacies F–G, comprising abundant Type III terrestrial organic matter (Hennissen *et al.* 2024), have relatively low C/N, whereas the marine facies have high C/N (Fig. 8). This discrepancy shows that C/N is a poor measure for organic matter type in these rocks (consistent with e.g. Mercuzot *et al.* 2021 and references therein).

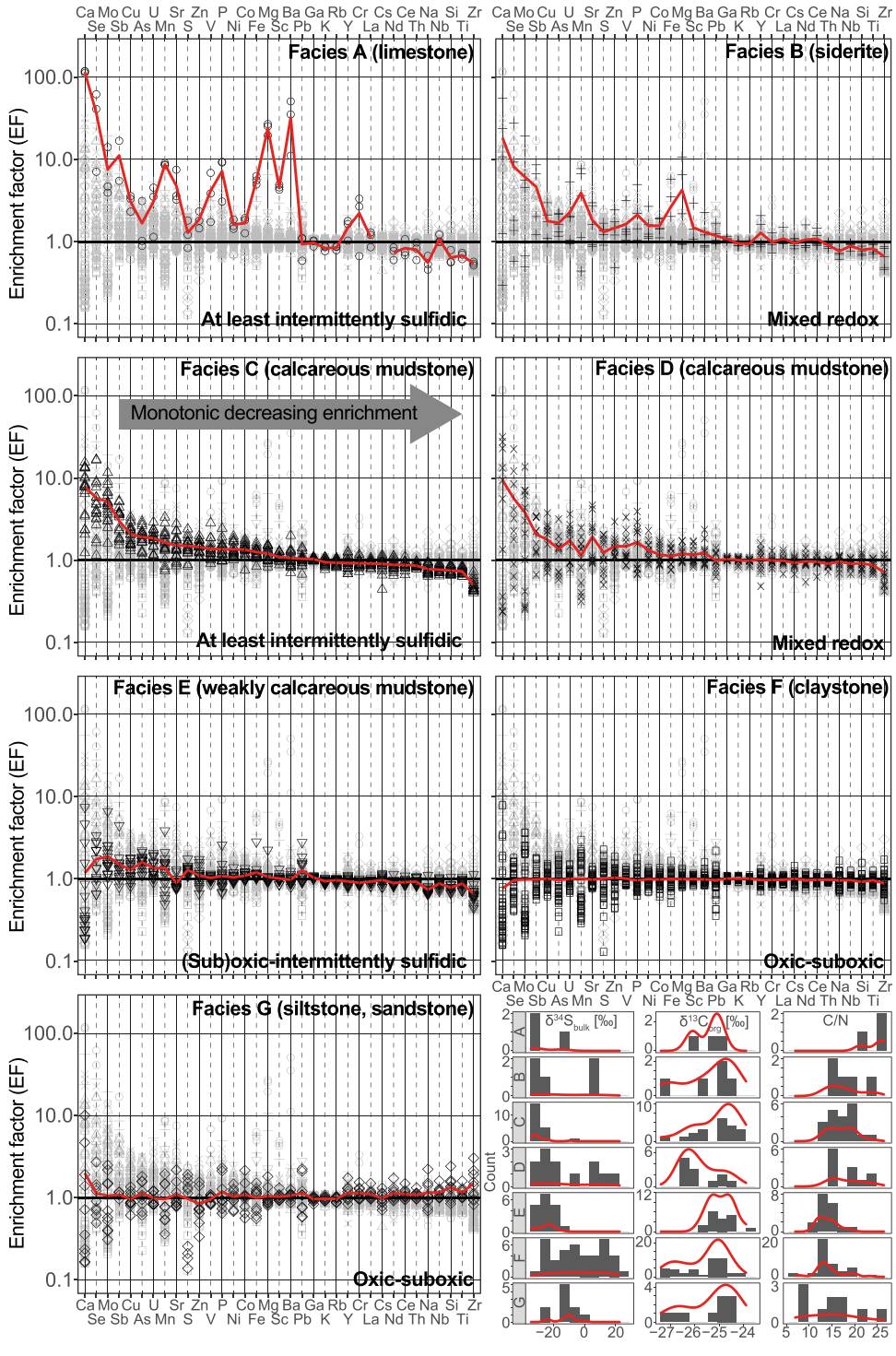

Fig. 8. Major- and trace-element enrichment factors for chemofacies A–G, normalized to the chemofacies F–G (oxic–suboxic) mean. Red lines for the enrichment factor plots are mean curves. Bottom right: $\delta^{34}S_{bulk}$, $\delta^{13}C_{org}$ and C/N histograms and density curves for chemofacies A–G.

Low C/N in argillaceous sediments (chemofacies F–G) is best explained by a quantitative contribution from inorganic (clay–bound) NH_4^+ (Lindgreen 1994), whereas high C/N in the anoxic facies is consistent with the preferential degradation of nitrogen-rich amino acids under suboxic conditions (Van Mooy *et al.* 2002).

Finally, dual assessment of S/TOC_o and Sr/Ba palaeosalinity proxies (Berner and Raiswell 1984; Wei and Algeo 2020), Mo v. U enrichment factors (Algeo and Tribovillard 2009; Tribovillard *et al.* 2012) and Mo v. TOC_o (Algeo and Lyons 2006) (Fig. 9a–c) provides further support for a weakly to moderately restricted, productivity-driven model for anoxia (Fig. 9d–g). Two samples exhibit S/TOC_o <0.1 at 1533.00 and 1536.36 m in core 1 (Figs 5 & 9a), which suggests the development of at least intermittently fully fresh bottom water conditions. The results of palynological analysis (Hennissen *et al.* 2024) support the sequence stratigraphic framework and model for anoxia. Marine transgressions often show a step-change from (1) proximal or marginal, (sub)oxic shelf edge palynofacies in the underlying lowstand packages into (2) anoxic shelf to basin palynofacies in each marine band package (Figs 4 & 5). The bioturbation analysis of Hennissen *et al.* (2024) is also consistent with the interpreted palaeoredox cyclicity.

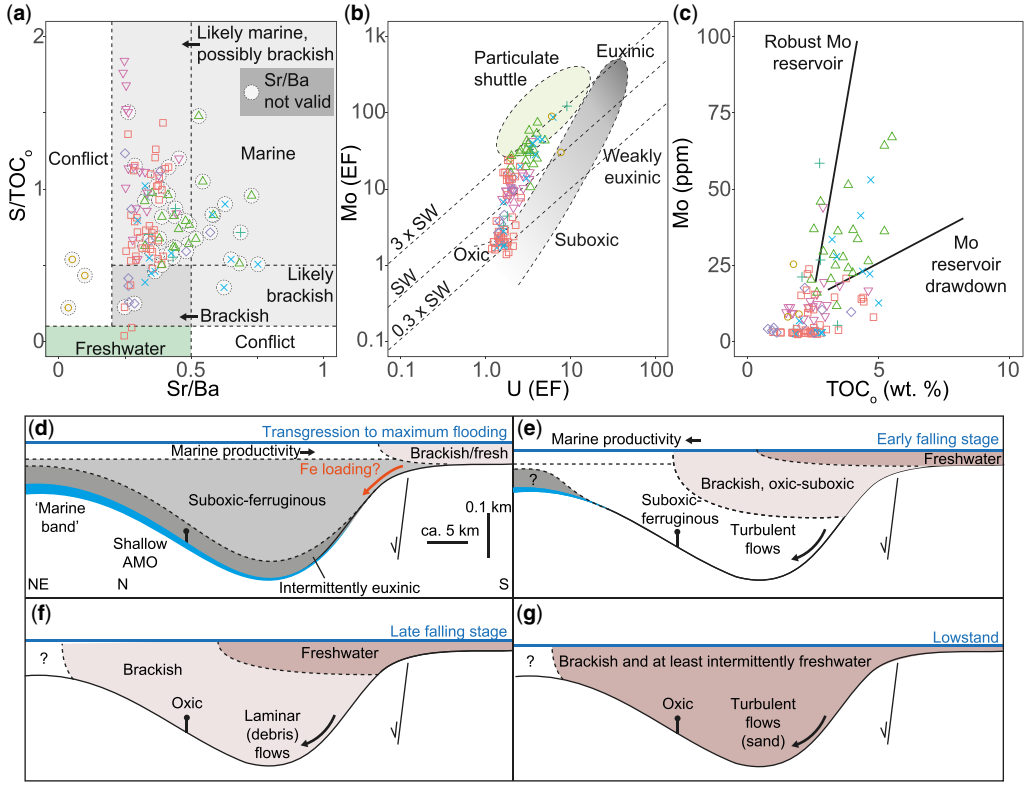

Fig. 9. Geochemical proxies for bottom water salinity and redox. (**a**) S/TOC (Berner and Raiswell 1984) and Sr/Ba (Wei and Algeo 2020) palaeosalinity proxies. Fields are bounded by the thresholds for salinity as defined in Wei and Algeo (2020), favouring the more widely established S/TOC proxy. Conflict zones could indicate decoupling between the S/TOC and/or Sr/Ba proxies, likely due to diagenetic effects. Circled data points exhibit inorganic C >0.3 wt%, a local threshold for Sr–bound and/or Ba-associated carbonate. In these cases, the Sr/Ba palaeosalinity proxy is invalid (Wei and Algeo 2020). (**b**) Mo v. U enrichment factors (EFs) (Algeo and Tribovillard 2009; Tribovillard *et al.* 2012) suggest fluctuation between oxygenated and weakly to moderately anoxic, intermittently sulfidic particulate shuttle conditions. (**c**) Mo v. TOC suggests deposition under weakly to moderately restricted bottom water conditions (Algeo and Lyons 2006). See 'Methods' for calculation of EFs and derivation of original TOC (TOC_o). (**d–g**) Interpreted redox and salinity response to fourth-order sea-level fluctuation, assuming productivity-driven anoxia in a weakly to moderately restricted basin (*sensu* Emmings *et al.* 2020*c*). The fourth-order cyclicity is partially overprinted by progradation of the Cefn-y-Fedw delta system. AMO, anaerobic oxidation of methane; TOC, total organic carbon.

Overall, the sedimentological observations, patterns of redox-sensitive metals and semi-metals both in core scan (Figs 4 & 5) and discrete (Fig. 8) samples, S and C stable isotopes, C/N and palynology (Fig. 8; Hennissen *et al.* 2024) support a model of productivity-driven marine anoxia (Emmings *et al.* 2020*c*). Anoxia was probably driven by productive marine phytoplankton and the export of highly labile organic matter into bottom waters, in a weakly to moderately restricted basin (Emmings *et al.* 2020*c*). Falling sea-level induced progradation of a freshwater lid into the Blacon Basin, a process that led to the shut–down in photic zone marine productivity and consequent basin ventilation, while generally sustaining normal marine or moderate salinities in bottom waters. Thus, the palaeosalinity record often lags the palaeoredox signal (Fig. 9). Based on S/TOC_o, bottom waters were fully desalinated only once, during a well-developed lowstand in the upper part of the Kinderscoutian section (core 1) (Fig. 5).

Stacking patterns and basin fill

Three kNN machine learning algorithms were deployed to predict siltstone and sandstone (chemofacies G), claystone and siderite (chemofacies F, B), calcareous mudstone (chemofacies C, D and E) and limestone (chemofacies A) through the Bowland Shale Formation in Ellesmere Port-1 (Fig. 10). Importantly, differentiation of non-calcareous and calcareous mudstone facies helps to interpret the succession in the context of syngenetic processes (Fig. 9d–g) and, ultimately, sequence stratigraphy. Based on these predictions, the Bowland Shale Formation comprises *c.* 18% siltstone and sandstone, 37% non-calcareous mudstone, 42% calcareous mudstone and 3% limestone. The unit comprises 12 complete fourth-order cycles, and is interfingered with the three distal Lower, Middle and Upper units (leaves) of the Cefn-y-Fedw Sandstone Formation (Davies *et al.* 2004; Waters *et al.* 2021).

Using the ammonoid biozonation in the two core sections together with the known age ranges of each of the distal turbidite leaves of the Cefn-y-Fedw Sandstone (Davies *et al.* 2004), it is possible to infer the key index regional marine bands (Davies *et al.* 2011) in the Blacon Basin. Like the observations in the core sections, generally sharp transitions from non-calcareous to calcareous mudstones are interpreted to indicate deposition during marine transgressions. Eight of the 12 cycles exhibit resolvable thin limestone beds, which probably coincide with the maximum rate of transgression and/or early part of the sea-level highstand. Thus, the Blacon Basin apparently preserves a largely complete Namurian succession, analogous to the Craven Basin (Saunders and Ramsbottom 1986). In all cycles, the calcareous mudstones are progressively or abruptly replaced with non-calcareous mudstones and/or siltstone to sandstone facies. We interpret these shifts from calcareous to siliciclastic facies to represent deposition during falling sea-level, culminating in lowstands. The abrupt transitions from calcareous to non-calcareous mudstones are analogous to observations in core (Figs 4 & 5): metre-scale cohesive debris flows shed from the basin margins. The Lower, Middle and Upper units of the Cefn-y-Fedw Sandstone Formation plausibly occupy the lowstands of multiple cycles and are potentially associated with erosional basal surfaces that cut into the underlying strata. We interpret deposition of the Middle Cefn-y-Fedw Sandstone unit to span and/or to have incised through the entirety of the Alportian in the Blacon Basin. Thus, the mass transport deposit underlying the $H_{1a}1$ marine band in core 2 (Fig. 4) probably represents a precursor or the first pulse of the Middle Cefn-y-Fedw Sandstone unit. Similarly, the siltstone facies at the top of the Kinderscoutian section (core 1) is interpreted as the base of the Upper Cefn-y-Fedw Sandstone unit (Fig. 5).

We integrated the sequence stratigraphic interpretations, based on the core scan observations and machine learning, with observations from other key wells in the Blacon Basin (Fig. 11). The results constrain the sedimentary architecture in the Blacon Basin. Ellesmere Port-1 is not located in the deepest part of the basin; it is located on the NE flank of the basin. Taking a basin-wide perspective shows the importance and influence of the Cefn-y-Fedw delta system; except for the relatively thin marine band facies, the Bowland Shale in the Blacon Basin is relatively expanded and totally dominated by prodeltaic mud (Fig. 11). This is consistent with the dominance of Type III organic matter (including large plant fragments) in both core sections (Hennissen *et al.* 2024). This contrasts with the Bowland Shale in the Craven Basin; whilst also supplied by a large delta system, the succession in the Craven Basin represents deposition from a more balanced mixture of competing hemipelagic (biogenic) and allochthonous components (Clarke *et al.* 2018; Newport *et al.* 2018; Emmings *et al.* 2020*a*, *b*, *c*). The relatively expanded, clay-rich and poorly cemented mudstone succession (Fig. 6) is also in contrast to the economically important, broadly time-equivalent Barnett Shale Formation (Loucks and Ruppel 2007). Ultimately, the structurally complex, collisional intercontinental setting explains why many of the US gas shales are poor analogues for the Bowland Shale. Structural complexity offers a direct challenge to unconventional hydrocarbon extraction from the Bowland Shale (Anderson and Underhill 2020), but is also implicated in the compartmentalization of key cemented

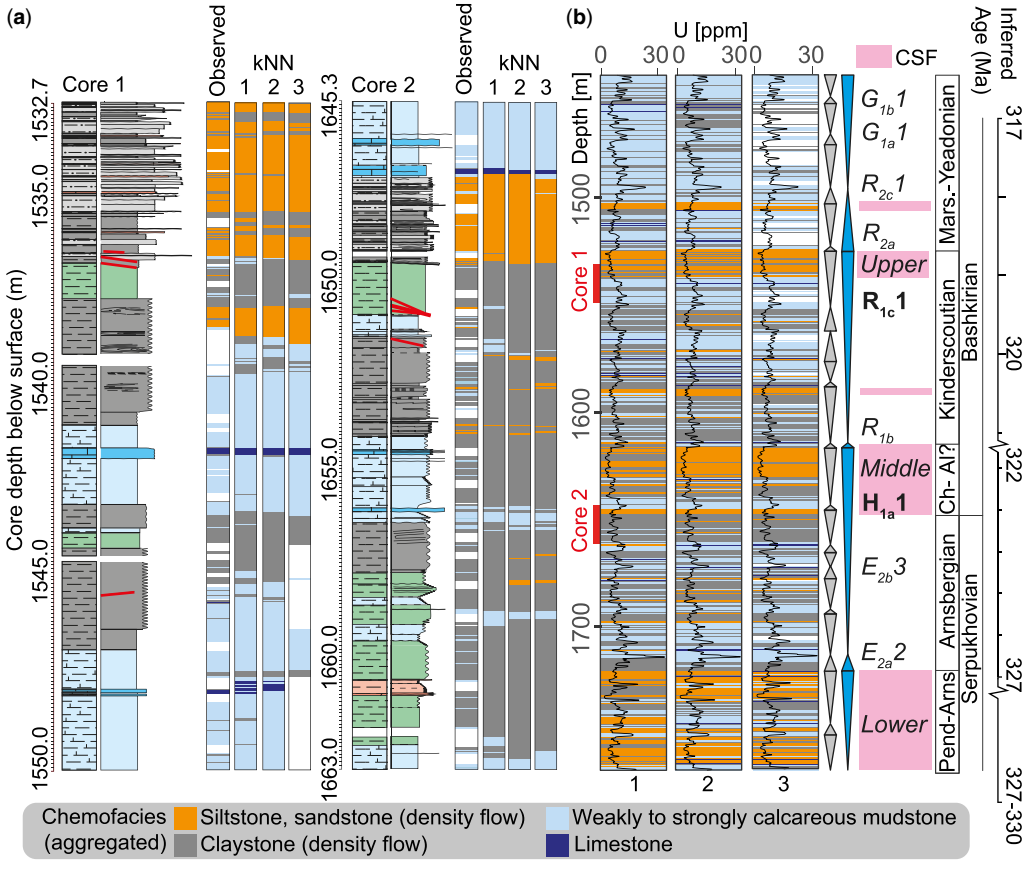

Fig. 10. The results of three KNN predictive chemofacies models. (**a**) Chemofacies were derived from principal component analysis and hierarchical cluster analysis of selected XRF core scan elements, simplified (aggregated) and matched to the nearest wireline datum. The models were trained and deployed by matching the XRF-derived chemofacies to selected wireline logs. kNN (1–3) represent different approaches (see 'Methods'). (**b**) The trained models were deployed on the observed Bowland Shale section at Ellesmere Port-1 (1443 to 1767 m below surface) (kNN method 2 is displayed). Prominent sand packages probably correspond to lower, middle and upper extensions of the Cefn-y-Fedw Sandstone (CSF) (Waters *et al.* 2021) coincident with three periods of regional channel incision (Waters and Condon 2012). Biostratigraphic ammonoid zones observed in core (bold), other inferred major flooding events and biozones (italicized, from Davies *et al.* 2011) and interpreted substages and extrapolated ages (Waters and Condon 2012) are also indicated.

lithofacies and the encroachment of delta systems linked to an uplifting hinterland.

The stratigraphic analysis delineates an inflection point immediately above the Middle Cefn-y-Fedw Sandstone turbidite package at *c.* 1615 m below surface, at or near the base of the Kinderscoutian (Fig. 10). The Pendleian and Arnsbergian cycles exhibit relatively low temporal frequency and a relatively low mSAR (e.g. condensed) and are more strongly asymmetrical, which is suggestive of deposition under the combined influence of eustatic sea-level fluctuation and basin subsidence (e.g. Martinsen *et al.* 1995). Waters *et al.* (2021) showed that, during the Pendleian–Arnsbergian, detrital sediments entered the Blacon Basin via the Cefn-y-Fedw delta systems in the SW (Fig. 11). Sediment flows were potentially aligned parallel to the long axis of the combined Blacon and Widnes basins (Fig. 1), analogous to the Gainsborough Trough (Palci *et al.* 2020). Whilst the age of the Middle Cefn-y-Fedw Sandstone turbidite package is poorly constrained (Waters *et al.* 2021), it: (1) is potentially Chokierian, Alportian and/or earliest Kinderscoutian in age, and therefore must span or juxtapose one or more significant hiatuses; (2) overlies the $H_{1a}1$ biozone, and therefore probably occurs within the mid-Carboniferous (Mississippian–Pennsylvanian) eustatic event (Saunders and Ramsbottom

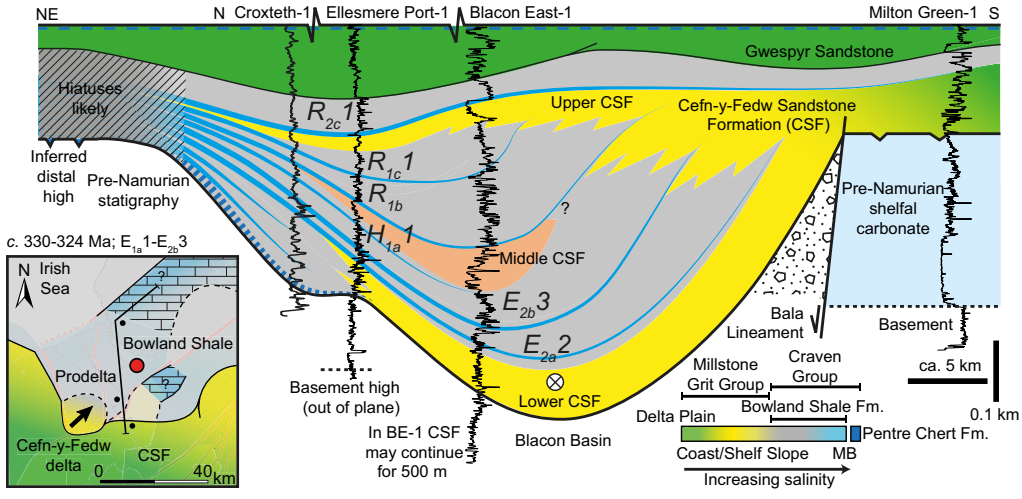

Fig. 11. Summary of interpreted Namurian sedimentary architecture in the Blacon Basin, with major flooding events of Davies *et al.* (2011) and general stratigraphy after Magraw and Ramsbottom (1957), Davies *et al.* (2004), Smith *et al.* (2005), Waters *et al.* (2009, 2021) and Andrews (2013). The shelf-edge delta wedge of the Late Pleistocene Po River (Adriatic Sea, offshore central Italy) may represent a partial (albeit short-lived) modern analogue (Pellegrini *et al.* 2017; Patruno and Helland-Hansen 2018). Gamma-ray well logs for Croxteth-1, Ellesmere Port-1 (this study), Blacon East-1 and Milton Green-1 are shown for reference. The line of section is flattened and truncated on a Yeadonian marine flooding surface (e.g., G_1 marine band) within the Gwespyr Sandstone. See Figure 1 for line of section. MB, marine band.

1986); and (3) is succeeded by a return to mud-dominated deposition in the early Kinderscoutian. Deposition of sand and the presence of hiatuses is consistent with the development of protracted low eustatic sea-level during the mid-Carboniferous event, which potentially shifted the main depocentres into deeper basins (e.g. the Craven Basin in the Irish Sea). Thus, the Middle Cefn-y-Fedw Sandstone could represent a turbidite lobe deposited during third-order sea-level regression associated with the mid-Carboniferous eustatic event, although the role of local controls such as fault reactivation is unresolved.

The lithostratigraphic analysis shows that the Blacon Basin became re-established as a major depocentre for mud during the Kinderscoutian. The well correlation together with heavy mineral analysis of Waters *et al.* (2021) suggests the Blacon Basin continued to receive detrital sediment from a single source via the Cefn-y-Fedw delta system, located in the south or SW. The Kinderscoutian to Yeadonian cycles apparently exhibit higher temporal frequency. Additionally, the Kinderscoutian–Yeadonian succession was deposited under a relatively high mSAR and the cycles are slightly more symmetrical, which probably reflects increasing proximity to the Cefn-y-Fedw delta front (Fig. 11). By the Yeadonian, sediment supply into the Blacon Basin became more complex, with provenances from the SW, SE, NW and NE (Waters *et al.* 2021).

RHP and heat flow

RHP calculations for the Bowland Shale in borehole Ellesmere Port-1 indicate bulk RHPs of 2.6 ± 1.3 μW m^{-3} (Fig. 12). Similarly high RHPs are also observed in the Bowland Shale in the Craven Basin. The Bowland Shale RHPs are significantly higher than the global shale mean of *c.* 1.5 μW m^{-3} reported by Vilà *et al.* (2010), and approach the RHPs of granitic intrusions, targeted for geothermal energy in the UK (Gluyas *et al.* 2018). RHP derives from the decay of U, K and Th, in descending order of importance (Rybach 1976). The U, K and Th data (Fig. 12c) indicate that the high RHPs are primarily due to relatively high U concentrations, whereas Th and K concentrations are broadly in line with the global average. The U contents are relatively but not absolutely high; for example, the Alum Shale (Sweden) exhibits U concentrations between 100 and 300 ppm (Lecomte *et al.* 2017), an order of magnitude greater than those found in the Bowland Shale.

The relatively high U in Carboniferous sedimentary rocks is additionally important because U can become mobile in groundwater or produced waters (Smedley *et al.* 2006), and the decay of U contributes to Rn risk areas where the rocks crop out (Miles *et al.* 2007). However, it should be noted the vast majority of UK groundwaters exhibit U concentrations far below the World Health Organization provisional

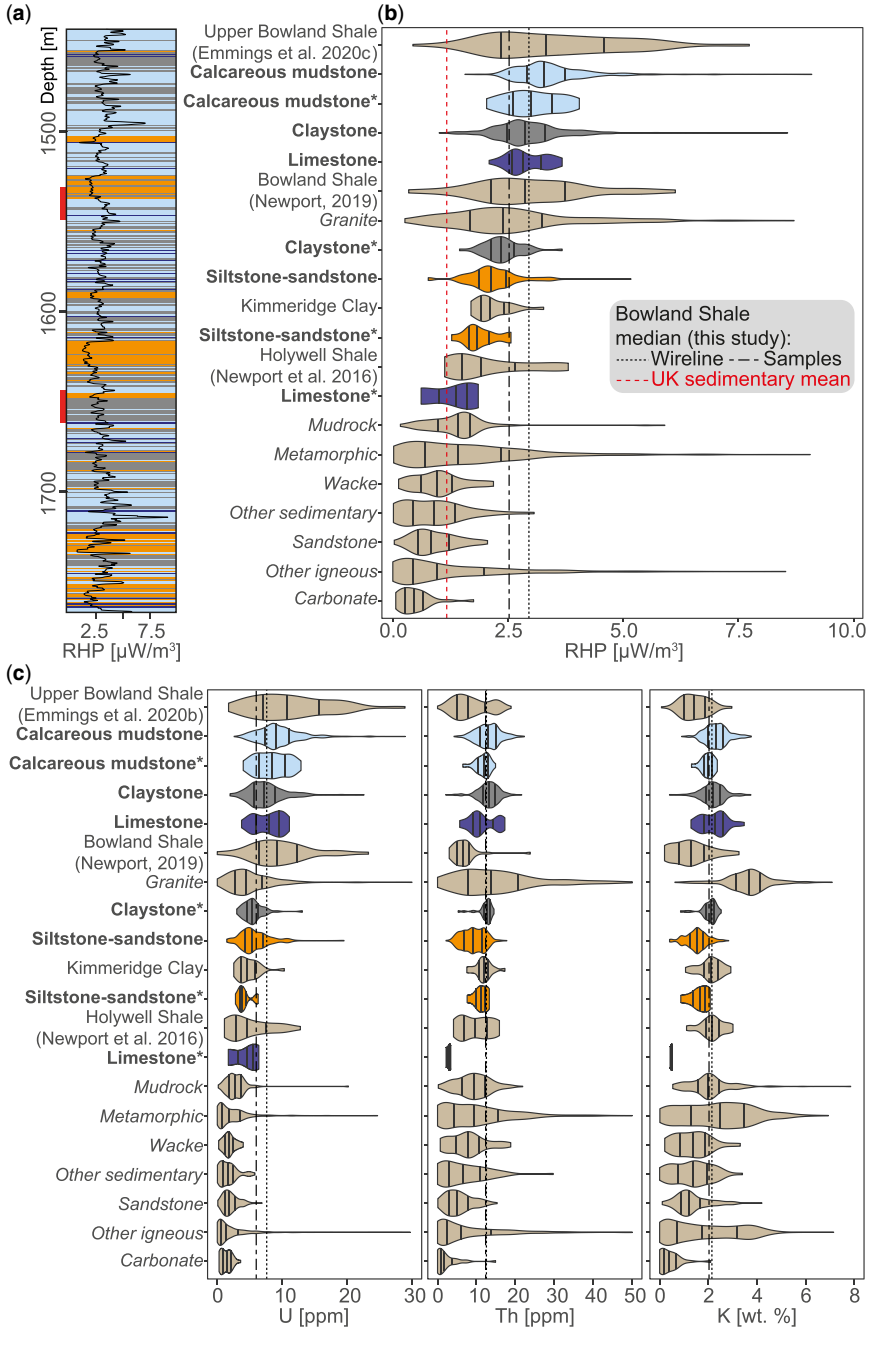

Fig. 12. Comparison of RHPs and U, Th and K concentrations for a range of rock types. (**a**) Calculated RHPs through the Bowland Shale based on the spectral gamma-ray well log data superimposed on the machine predictions. (**b**, **c**) RHPs and U, Th and K concentrations for limestone, claystone, calcareous mudstone and siltstone–sandstone facies in the Bowland Shale in Ellesmere Port-1, based on spectral gamma-ray and discrete XRF analysis (the latter indicated by asterisks). The UK RHP sedimentary mean (Rollin 2002; Busby and Terrington 2017) and RHPs for the Bowland Shale in the Craven Basin (Newport 2019; Emmings *et al.* 2020*c*), the Kimmeridge Clay (Elm Tree Farm, Yorkshire, J.F.E. unpublished borehole data/analyses), Holywell Shale (Newport *et al.* 2016) and italicized baseline data (Vilà *et al.* 2010) are also shown.

guideline value for U in drinking water (15 μg l^{-1}) (Smedley *et al.* 2006). Additionally, the relatively high U contents in UK groundwaters commonly derive from sandstone red-beds, rather than Carboniferous shales, and U mobility is dependent on the mineral host and speciation (e.g. Smedley *et al.* 2006; Phan *et al.* 2015). From a regional perspective, U in the Bowland Shale is primarily hosted in recalcitrant mineral or organic phases (Parnell *et al.* 2022, see below) and is therefore likely to be relatively immobile.

The relatively high U contents observed in the Bowland Shale are potentially explained by three factors. Firstly, high U concentrations are a general feature of Devonian–Carboniferous shales globally (Mehra *et al.* 2021), suggesting a first-order, fundamental change in the availability and/or fixation pathway of U in marine sediments during this time interval. Secondly, a productivity-driven model for anoxia and high mSARs related to proximity to multiple delta systems probably promoted under-consolidation of seabed sediments during deposition of the Bowland Shale. Since U is primarily fixed within porewaters, rather than bottom waters (Tribovillard *et al.* 2006), under-consolidation could plausibly promote U drawdown due to generally enhanced shallow sediment porosity and diffusivity with bottom waters. Finally, the siltstone and sandstone facies in the Bowland Shale also exhibit high RHPs above the global sandstone average (Fig. 12). This strongly suggests an important role of provenance; granitic rocks were present in the hinterland (Waters *et al.* 2021) and the siltstones in Ellesmere Port-1 are compositionally immature, consistent with a granitic provenance. Specifically, silt and sand in the Bowland Shale is enriched in a suite of detrital minerals that are important hosts of U in granite (Nash 1979), including heavy minerals, mica and especially detrital magnetite (Emmings *et al.* 2020*c*).

We modelled a range of scenarios using the heat flow box model equations of Beardsmore *et al.* (2010), assuming complete isotropy and negligible convective heat transport. Conductive heat flow is controlled by two parameters (Beardsmore *et al.* 2010): *in situ* RHP (Rybach 1976) and the thermal conductivity of constituent phases. Carbonates, clay minerals and unsaturated or saturated pores are thermal insulators, whereas pyrite and quartz are important thermal conductors (Midttømme *et al.* 1998; Midttømme and Roaldset 1999). The distribution of these phases in black shales is synergistically linked to redox conditions during deposition and diagenesis and is therefore predictable (Fig. 9) (Emmings *et al.* 2020*b*, *c*).

The models show that heat flow is highly sensitive to thermal conductivity and is minimally affected by RHP (supplementary material B, see following discussion). Thus, black ('hot') shales are unlikely to represent a credible, direct target for geothermal energy. However, the Bowland Shale could act as an effective thermal blanket to underlying geothermal reservoirs (e.g. Nunn *et al.* 1999). This effect is potentially manifested as the Bowland Forest heat anomaly described by Lee *et al.* (1987), although the anomaly is not identified in more recent mapping (e.g. Busby 2014). Maintaining the same arbitrary surface heat flow (50 W m^{-2}) and RHP (3 μW m^{-3}), box modelling shows that the base of a 1 km-thick claystone unit is *c.* 17°C warmer than at the base of a 1 km-thick siliceous, pyritic mudstone unit. This is because clay minerals are insulators whereas quartz and pyrite are conductors of heat. In these models, we assumed the same *in situ* RHP of 3 μW m^{-3} (Fig. 12b), which results in a relatively small excess temperature gradient of 0.75°C km^{-1}. However, adopting an *in situ* RHP of 10 μW m^{-3} that is more comparable to high-RHP granite (Vilà *et al.* 2010) imparts an excess temperature gradient of 2°C km^{-1}. Thus, RHP becomes quantitively important where it is consistently high in a large rock volume (e.g. granite batholiths), a feature that is unlikely to be observed in sedimentary basins because it requires the presence of extremely thick metalliferous black shale packages. Whilst these modelling exercises are not entirely realistic, this approach helps to demonstrate the importance of understanding mudstone lithofacies as a control on subsurface heat flow.

In another exercise, we fitted two different, similarly accurate (but not necessarily realistic) temperature gradient models through the Bowland Shale in Ellesmere Port-1 (Fig. 13; supplementary material B). Whilst the measured borehole temperatures in Ellesmere Port-1 are unlikely to be equilibrated with the surrounding rock, the data delineate the key inflection at *c.* 1615 m interpreted as related to the mid-Carboniferous eustatic event and delta progradation (see prior discussion). This inflection differentiates geothermal gradients of *c.* 25°C km^{-1} and 18°C km^{-1}, respectively. Model 1 is based on a single, homogeneous, low-conductivity claystone package with low RHP (1.5 μW m^{-3}), 5% total porosity (Clarke *et al.* 2018), 80% clay minerals, 10% quartz and 5% carbonate minerals. Model 1 requires relatively low heat flows of 62 and 42 mW m^{-2}, above and below 1615 m below surface, respectively, to match the observed borehole temperature profile. Model 2 is based on the calculated RHPs and machine predicted thicknesses and composition of each discrete package within the Bowland Shale (Figs 10 & 13), and is therefore considered more realistic. In model 2, thermal conductivities are higher in all facies, which necessitate higher heat flows of 75 and 55 mW m^{-2}, above and below 1615 m below surface, respectively. Thus, based on the observations coupled to modelling,

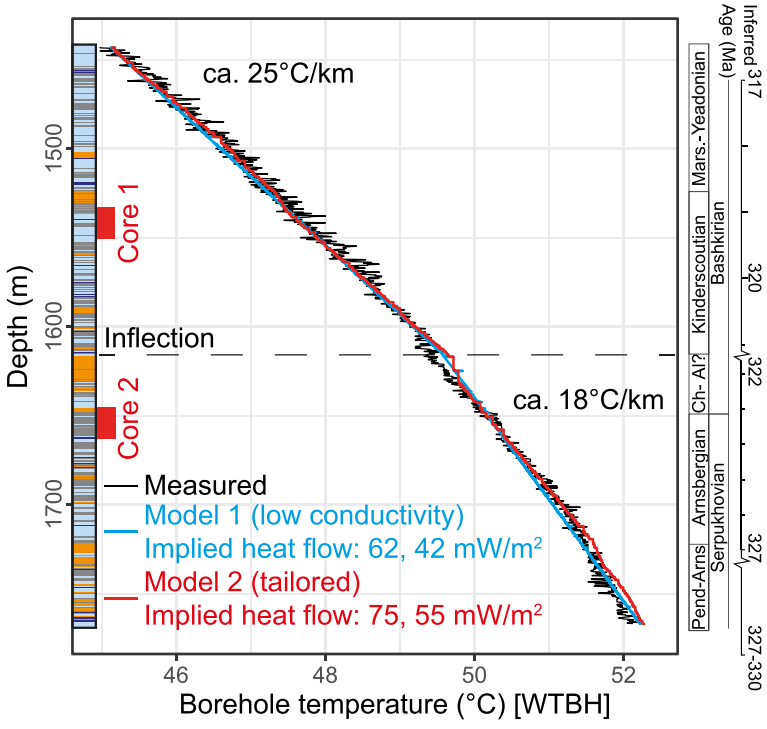

Fig. 13. Measured v. modelled temperature gradients through the Bowland Shale Formation in Ellesmere Port-1. It should be noted the borehole temperatures are unlikely to represent true, equilibrated values and therefore probably represent minimum estimates.

the Bowland Shale in Ellesmere Port-1 is not necessarily an effective thermal 'blanket' since it comprises *c.* 18% siltstone and sandstone, and instead may conduct heat at a faster rate (i.e. high thermal diffusivity) than pure claystones or condensed organic-rich shales. Again, these models are likely to be overly simplistic but demonstrate the importance of understanding the fractions of different mudstone facies within a given 'shale' package. The models do not consider the effect of organic matter (particularly coal) and are limited to the classes (lithologies) observed in the two cored sections. In particular, coals were not observed in either core section, but coal exhibits a very low thermal conductivity (Nunn and Lin 2002) and coal seams are present in the Bowland Shale in North Wales (Davies *et al.* 2004).

The Blacon Basin, in addition to many other sedimentary basins, is filled by hundreds of metres of Carboniferous mudstone. Important UK geothermal plays include granites (Gluyas *et al.* 2018) and karstified Carboniferous limestones (Busby 2014). Carboniferous limestone–mudstone cyclothems cap granites on several blocks (e.g. proven in the Rydale and Rookhope boreholes; Dunham and Wilson 1985) and cap lower Carboniferous limestones in the UK (e.g. Fig. 10; Dunham and Wilson 1985; Busby 2014). Additionally, basinal Carboniferous mudstones may cap granites beneath local intrabasin highs (Bott 1988; Donato 2020). Yet, our ability to explore for deep geothermal energy in sedimentary basins is limited by a lack of understanding of how different types of shales control heat flow. Efficient heat diffusion is also important for the safe geological storage of radioactive waste (Rutqvist 2020), and the design of heat pumps is dependent on the thermal properties of the storage medium (Busby *et al.* 2009; Parkes *et al.* 2021). Simple box modelling together with previous work (e.g. Midttømme *et al.* 1998) shows that the efficiency of the sedimentary thermal blanket is highly dependent on mudstone mineralogy and, by extension, lithofacies. Therefore, future work should seek to: (1) measure the key thermal properties for a range of mudstone microfacies; (2) better understand the role of depositional processes, basin type and age as controls on mudstone facies coupled to thermal conductivity; (3) constrain the effect of diagenesis on mudstone thermal properties; (4) link the thermal properties of mudstones to one or more holistic, predictive frameworks (e.g. sequence stratigraphy); and (5) investigate the potential for convective fluid flow through fracture networks,

which are more likely to be developed within relatively brittle mudstone microfacies (e.g. siliceous and carbonate-cemented marine band facies).

Conclusions

We conducted a high-resolution multi-disciplinary analysis of two core sections in the borehole Ellesmere Port-1, Cheshire, UK. Biostratigraphic analysis indicates the core sections are Kinderscoutian and late Arnsbergian–Chokierian in age, respectively. Both cores are assigned to the Bowland Shale Formation. Coupled core scan and discrete geochemical analysis enables interpretation of syngenetic processes at a relatively high temporal resolution (*c.* 1–2 kyr). Both cores comprise cycles of limestone, calcareous to non-calcareous mudstone and siltstone that are characteristic of the Bowland Shale in the UK. The cycles are interpreted to represent sediment deposition during fourth-order, glacioeustatic sea-level fluctuation. Palaeoredox and palaeosalinity geochemical proxies support a model for productivity–driven anoxia in a weakly to moderately restricted basin. Coupled Mo/Al and As/Al core scan ratios support a model for intermittently euxinic bottom waters overlain by relatively thick ferruginous intermediate waters. Falling sea-level led to waning marine productivity; euxinic bottom waters were progressively replaced with ferruginous waters, followed by the development of fully suboxic or oxic conditions during the late falling stage and lowstands.

Unlike the Pendleian Bowland Shale in the Craven Basin, the cored Bowland Shale successions in Ellesmere Port-1 are not siliceous and are instead dominated by argillaceous mudstones. Marine band facies are interpreted to represent deposition during marine transgressions and highstands. Falling sea-level is linked to the progressive or abrupt replacement of calcareous mudstones with siliciclastic (non–carbonate-bearing) claystones. The siliciclastic mudstones are commonly laminated and often exhibit chaotic sedimentary structures, suggestive of deposition from a range of density flow types, including potential for en masse transport within debris flows. Laminated siltstone and sandstone packages occasionally cap the siliciclastic claystones and are interpreted to represent deposition during lowstands, where bottom water conditions were unambiguously oxygenated, brackish and at least intermittently freshwater.

Cluster analysis of the XRF core scan data coupled to machine learning of the well log data enabled prediction of limestone, calcareous mudstone, siliciclastic (non-carbonate) claystone, and siltstone and sandstone facies through the entire Bowland Shale interval in Ellesmere Port-1. The machine predictions show that the Bowland Shale is interfingered with the three turbiditic leaves of the Cefn-y-Fedw Sandstone and contains 12 complete fourth-order cycles resolvable in the well log data. The Bowland Shale comprises *c.* 18% siltstone and sandstone, 37% non-calcareous mudstone, 42% calcareous mudstone and 3% limestone. A step-change in the symmetry and thickness of cycles at *c.* 1615 m below surface probably corresponds to an important regional shift in the rate of sediment supply from the Cefn-y-Fedw delta system, above the mid-Carboniferous boundary.

The Bowland Shale exhibits high RHP in comparison to other sedimentary rocks, due primarily to relative enrichment in U. Despite this, box model heat modelling calibrated to borehole temperature measurements show that heat flow is minimally influenced by the high RHP in the Bowland Shale. Modelling suggests that it is not necessarily appropriate to assume that the Bowland Shale acts an insulating blanket over subsurface heat flow. Simple box modelling shows that the efficiency of the sedimentary thermal blanket is highly dependent on mudstone mineralogy and facies. The Bowland Shale in the Blacon Basin is relatively expanded and does not represent a highly condensed black shale unit. Based on the compositional (XRF) analysis, the Bowland Shale microfacies in the UK are likely to be more conductive than a simple claystone lithology. Considering the potential importance of Carboniferous mudstones as caprocks to buried granite and limestone geothermal plays in the UK, further work should: (1) measure the thermal properties of a range of mudstone microfacies; and (2) link the findings to established depositional and lithostratigraphic models to better understand the extent to which mudstone units act as thermal blankets.

Acknowledgements We acknowledge the National Geoscience Data Centre (NGDC), British Geological Survey for enabling access to the Ellesmere Port-1 core materials. We acknowledge Mike Stephenson (formerly BGS) for helping to facilitate the research project. We thank Simon Harris (BGS) and Sarah Davies (University of Leicester) for facilitating access to laboratory facilities at the NGDC and the University of Leicester XRF laboratory, respectively. Contains data supplied by permission of the Natural Environment Research Council [2022]. Contains information provided by the Oil and Gas Authority and/or other third parties. We are grateful to the reviewers for helping to improve this manuscript through their valuable comments.

Competing interests The authors declare that they have no known competing financial interests or personal relationships that could have appeared to influence the work reported in this paper.

Author contributions **JFE**: conceptualization (lead), data curation (lead), formal analysis (lead), methodology (lead), visualization (lead), writing – original draft (lead), writing – review & editing (lead); **JAIH**: data curation (lead), formal analysis (lead), methodology (lead), visualization (supporting), writing – original draft (supporting); **CHV**: formal analysis (supporting), resources (supporting), supervision (supporting); **MD**: data curation (lead), formal analysis (lead), resources (supporting), writing – original draft (supporting); **LM**: formal analysis (lead); **VM-H**: formal analysis (supporting); **AL**: formal analysis (lead), writing – original draft (supporting); **JL**: formal analysis (lead), writing – original draft (supporting); **ML**: funding acquisition (supporting), resources (supporting), supervision (supporting); **NJR**: formal analysis (supporting).

Funding This research was primarily funded by a British Geological Survey (UKRI) National Capability grant NEE6640S (to JFE). JAIH is supported by the Natural Environment Research Council through the Unconventional Hydrocarbons in the UK Energy System Programme (UKUH) Challenge 2 (NE/R017964/1). Stable C isotope analyses were funded by the NEIF Steering Committee [grant no. IP-1918-0619] (to MJL).

Data availability All discrete sample geochemical datasets (Rock-Eval pyrolysis, XRF elemental analysis, stable C and S isotopes) are reported in the Supplementary material. The XRF core scan dataset is archived and openly available via the NDGC (BGS Core Scanning Facility 2022). The Ellesmere Port-1 cores are openly available via the National Geoscience Data Centre (NGDC), British Geological Survey. Well log data are available via the National Data Repository (https://www.nstauthority.co.uk/data-centre/access-to-information-and-samples/). The palynology and vitrinite reflectance datasets are reported by Hennissen *et al.* (2024).

References

Aitchison, J. 1986. *The Statistical Analysis of Compositional Data*. Chapman & Hall, London.

Algeo, T.J. 2004. Can marine anoxic events draw down the trace element inventory of seawater? *Geology*, **32**, 1057–1060, https://doi.org/10.1130/G20896.1

Algeo, T.J. and Lyons, T.W. 2006. Mo–total organic carbon covariation in modern anoxic marine environments: implications for analysis of paleoredox and paleohydrographic conditions. *Paleoceanography and Paleoclimatology*, **21**, https://doi.org/10.1029/2004PA001112

Algeo, T.J. and Tribovillard, N. 2009. Environmental analysis of paleoceanographic systems based on molybdenum–uranium covariation. *Chemical Geology*, **268**, 211–225, https://doi.org/10.1016/j.chemgeo.2009.09.001

Algeo, T.J., Heckel, P.H., Maynard, J.B., Blakey, R. and Rowe, H. 2008. Modern and ancient epeiric seas and the super-estuarine circulation model of marine anoxia. *GSA Special Papers*, **48**, 7–38.

Anderson, I. and Underhill, J.R. 2020. Structural constraints on Lower Carboniferous shale gas exploration in the Craven Basin, NW England. *Petroleum Geoscience*, **26**, 303–324, https://doi.org/10.1144/petgeo2019-125

Andrews, I.J. 2013. *The Carboniferous Bowland Shale Gas Study: Geology and Resource Estimation*. British Geological Survey for Department of Energy and Climate Change.

Arthurton, R.S. 1984. The Ribblesdale fold belt, NW England – a Dinantian–early Namurian dextral shear zone. *Geological Society, London, Special Publications*, **14**, 131–138, https://doi.org/10.1144/GSL.SP.1984.014.01.13

Auguie, B. 2016. *gridExtra* R package version 2.2.1, https://CRAN.R-project.org/package=gridExtra

Baines, J.G. 1977. *The Stratigraphy and Sedimentology of the Skipton Moor Grits (Namurian E_{1c}) and their Lateral Equivalents*. PhD thesis, University of Keele.

Beardsmore, G., Rybach, L., Blackwell, D. and Baron, C. 2010. A protocol for estimating and mapping global EGS potential. *Geothermal Resources Council Transactions*, **34**, 301–312.

Berner, R.A. and Raiswell, R. 1984. C/S method for distinguishing freshwater from marine sedimentary rocks. *Geology*, **12**, 365–368, https://doi.org/10.1130/0091-7613(1984)12<365:CMFDFF>2.0.CO;2

BGS Core Scanning Facility 2022. Ellesmere Port-1 Core Scanning Dataset. NERC EDS National Geoscience Data Centre.

Bloxam, T.W. and Thomas, R.L. 1968. Palaeontological and geochemical facies in the *Gastrioceras subcrenatum* marine-band and associated rocks from the North Crop of the South Wales Coalfield. *Quarterly Journal of the Geological Society*, **124**, 239–277, https://doi.org/10.1144/gsjgs.124.1.0239

Bott, M.H.P. 1988. The Market Weighton gravity anomaly; granite or graben? *Proceedings of the Yorkshire Geological Society*, **47**, 47–53, https://doi.org/10.1144/pygs.47.1.47

Bouch, J.E., Naden, J. *et al.* 2006. Direct evidence of fluid mixing in the formation of stratabound Pb–Zn–Ba–F mineralisation in the Alston Block, North Pennine Orefield (England). *Mineralium Deposita*, **41**, 821–835, https://doi.org/10.1007/s00126-006-0093-3

Brandon, A., Riley, N.J., Wilson, A.A. and Ellison, R.A. 1995. Three new early Namurian (E_{1c}-E_{2a}) marine bands in central and northern England, UK, and their bearing on correlations with the Askrigg Block. *Proceedings of the Yorkshire Geological and Polytechnic Society*, **50**, 333–355, https://doi.org/10.1144/pygs.50.4.333

Brogan, J.C., Fleming, G.A. and Byrne, J.E. 1973. Molybdenum and copper in Irish pasture soils. *Irish Journal of Agricultural Research*, **12**, 71–81.

Busby, J. 2014. Geothermal energy in sedimentary basins in the UK. *Hydrogeology Journal*, **22**, 129–141, https://doi.org/10.1007/s10040-013-1054-4

Busby, J. and Terrington, R. 2017. Assessment of the resource base for engineered geothermal systems in Great Britain. *Geothermal Energy*, **5**, 7, https://doi.org/10.1186/s40517-017-0066-z

Busby, J., Lewis, M., Reeves, H. and Lawley, R. 2009. Initial geological considerations before installing ground

source heat pump systems. *Quarterly Journal of Engineering Geology and Hydrogeology*, **42**, 295–306, https://doi.org/10.1144/1470-9236/08-092

Church, K.D. and Gawthorpe, R.L. 1994. High resolution sequence stratigraphy of the late Namurian in the Widmerpool Gulf (East Midlands, UK). *Marine and Petroleum Geology*, **11**, 528–544, https://doi.org/10.1016/0264-8172(94)90066-3

Clarke, H., Turner, P., Bustin, R.M., Riley, N. and Besly, B. 2018. Shale gas resources of the Bowland Basin, NW England: a holistic study. *Petroleum Geoscience*, **24**, 287–322, https://doi.org/10.1144/petgeo2017-066

Clarke, H., Verdon, J.P., Kettlety, T., Baird, A.F. and Kendall, J.M. 2019. Real-time imaging, forecasting, and management of human-induced seismicity at Preston New Road, Lancashire, England. *Seismological Research Letters*, **90**, 1902–1915, https://doi.org/10.1785/0220190110

Cózar, P. and Somerville, I.D. 2021. The Serpukhovian in Britain: use of foraminiferal assemblages for dating and correlating. *Journal of the Geological Society, London*, **178**, https://doi.org/10.1144/jgs2020-170

Davies, J.R., Wilson, D. and Williamson, I.T. 2004. *Geology of the Country around Flint*. Memoirs of the British Geological Survey, Sheet 108 (England and Wales).

Davies, J.R., Somerville, I.D., Waters, C.N. and Jones, N.S. 2011. North Wales. *In*: Waters, C.N., Somerville, I.D. *et al*. (eds) *A Revised Correlation of Carboniferous Rocks in the British Isles*. Geological Society, London.

Davies, R.J., Austin, R. and Moore, D. 1993. Environmental controls of Brigantian conodont-distribution: evidence from the Gayle limestone of the Yoredale Group in Northern England. *Annales de la Société géologique de Belgique*, **116**, 221–241.

Davies, S.J. 2008. The record of Carboniferous sea-level change in low-latitude sedimentary successions from Britain and Ireland during the onset of the late Paleozoic ice age. *GSA Special Papers*, **441**, 187–204, https://doi.org/10.1130/2008.2441(13)

Davies, S., Hampson, G., Flint, S. and Elliott, T. 1999. Continental-scale sequence stratigraphy of the Namurian, Upper Carboniferous and its applications to reservoir prediction. *Geological Society, London, Petroleum Geology Conference Series*, **5**, 757–770, https://doi.org/10.1144/0050757

Davydov, V.I., Korn, D. and Schmitz, M. 2012. The Carboniferous Period. *In*: Gradstein, F.M., Ogg, J.G., Schmitz, M.D. and Ogg, G.M. (eds) *The Geologic Time Scale 2012*. Elsevier, 603–651, https://doi.org/10.1016/B978-0-444-59425-9.00023-8

Dean, M.T., Browne, M.A.E., Waters, C.N. and Powell, J.H. 2011. A lithostratigraphical framework for the Carboniferous successions of northern Great Britain (Onshore). British Geological Survey Research Report **RR/10/07**.

DECC 2013. *The Hydrocarbon Prospectivity of Britain's Onshore Basins*. Department for Energy and Climate Change.

Dmitrijeva, M., Cook, N.J. *et al*. 2020. Multivariate statistical analysis of trace elements in pyrite: prediction, bias and artefacts in defining mineral signatures. *Minerals*, **10**, 61, https://doi.org/10.3390/min10010061

Donato, J. 2020. *Gravity Modelling Across Two Postulated Granite Batholiths within the UK Onshore East Midlands Shelf*. University of Oxford/UKOGL Beneath Britain.

Dowey, P.J. and Taylor, K.G. 2020. Diagenetic mineral development within the Upper Jurassic Haynesville-Bossier Shale, USA. *Sedimentology*, **67**, 47–77, https://doi.org/10.1111/sed.12624

Dowle, M. and Srinivasan, A. 2020. *data.table* R package version 1.13.2, https://CRAN.R-project.org/package=data.table

Droxler, A.W. and Schlager, W. 1985. Glacial v. interglacial sedimentation rates and turbidite frequency in the Bahamas. *Geology*, **13**, 799–802, https://doi.org/10.1130/0091-7613(1985)13<799:GVISRA>2.0.CO;2

Dunham, A.C. and Wilson, A.A. 1985. *Geology of the Northern Pennine Orefield: Volume 2, Stainmore to Craven*. Economic Memoir of the British Geological Survey.

Ellis, D. and Singer, J. 2007. *Well Logging for Earth Scientists*. Springer, Dordrecht.

Emmings, J.F. 2018. *Controls on UK Lower Namurian Shale Gas Prospectivity: Understanding the Spatial and Temporal Distribution of Organic Matter in Siliciclastic Mudstones*. PhD thesis, University of Leicester.

Emmings, J.F., Hennissen, J.A.I. *et al*. 2019. Controls on amorphous organic matter type and sulphurization in a Mississippian black shale. *Review of Palaeobotany and Palynology*, **268**, 1–18, https://doi.org/10.1016/j.revpalbo.2019.04.004

Emmings, J.F., Davies, S., Vane, C.H., Moss-Hayes, V. and Stephenson, M. 2020*a*. From marine bands to hybrid flows: sedimentology of a Mississippian black shale. *Sedimentology*, **67**, 261–304, https://doi.org/10.1111/sed.12642

Emmings, J.F., Dowey, P.I. *et al*. 2020*b*. Origin and implications of early diagenetic quartz in the Mississippian Bowland Shale Formation, Craven Basin, UK. *Marine and Petroleum Geology*, **120**, https://doi.org/10.1016/j.marpetgeo.2020.104567

Emmings, J.F., Poulton, S.W. *et al*. 2020*c*. A Mississippian black shale record of redox oscillation in the Craven Basin, UK. *Palaeogeography, Palaeoclimatology, Palaeoecology*, **538**, https://doi.org/10.1016/j.palaeo.2019.109423

Emmings, J.F., Poulton, S.W. *et al*. 2022. Pyrite meganalysis reveals modes of anoxia through geological time. *Science Advances*, **8**, eabj5687, https://doi.org/10.1126/sciadv.abj5687

Fauchille, A.L., Ma, L. *et al*. 2017. An enhanced understanding of the Basinal Bowland shale in Lancashire (UK), through microtextural and mineralogical observations. *Marine and Petroleum Geology*, **86**, 1374–1390, https://doi.org/10.1016/j.marpetgeo.2017.07.030

Fauchille, A.L., van den Eijnden, A.P. *et al*. 2018. Variability in spatial distribution of mineral phases in the Lower Bowland Shale, UK, from the mm- to µm-scale: quantitative characterization and modelling. *Marine and Petroleum Geology*, **92**, 109–127, https://doi.org/10.1016/j.marpetgeo.2018.02.029

Fisher, Q.J. and Wignall, P.B. 2001. Palaeoenvironmental controls on the uranium distribution in an Upper Carboniferous black shale (*Gastrioceras listeri* Marine Band) and associated strata; England. *Chemical Geology*, **175**, 605–621, https://doi.org/10.1016/S0009-2541(00)00376-4

Fraser, A.J. and Gawthorpe, R.L. 1990. Tectono-stratigraphic development and hydrocarbon habitat of the Carboniferous in northern England. *Geological Society, London, Special Publications*, **55**, 49–86, https://doi.org/10.1144/GSL.SP.1990.055.01.03

Fraser, A.J. and Gawthorpe, R. 2003. An Atlas of Carboniferous basin evolution in Northern England. *Geological Society, London, Memoirs*, **28**, https://doi.org/10.1144/GSL.MEM.2003.028

Fraser, A.J., Nash, D.F., Steele, R.P., Ebdon, C.C. and Fraser, A.J. 1990. A regional assessment of the intra-Carboniferous play of Northern England. *Geological Society, London, Special Publications*, **50**, 417–440, https://doi.org/10.1144/GSL.SP.1990.050.01.26

Gadd, M.G., Peter, J.M. *et al*. 2020. A Middle Devonian basin-scale precious metal enrichment event across northern Yukon (Canada). *Geology*, **48**, 242–246, https://doi.org/10.1130/G46874.1

Gluyas, J., Adams, C.A. *et al*. 2018. Keeping warm: a review of deep geothermal potential of the UK. *Proceedings of the Institution of Mechanical Engineers, Part A: Journal of Power and Energy*, **232**, 115–126, https://doi.org/10.1177/0957650917749693

Green, P.F., Duddy, I.R. and Bray, R.J. 1997. Variation in thermal history styles around the Irish Sea and adjacent areas: implications for hydrocarbon occurrence and tectonic evolution. *Geological Society, London, Special Publications*, **124**, 73–93, https://doi.org/10.1144/GSL.SP.1997.124.01.06

Gross, D., Sachsenhofer, R.F. *et al*. 2015. Organic geochemistry of Mississippian shales (Bowland Shale Formation) in central Britain: implications for depositional environment, source rock and gas shale potential. *Marine and Petroleum Geology*, **59**, 1–21, https://doi.org/10.1016/j.marpetgeo.2014.07.022

Hamilton, N. 2017. *ggtern* R package version 2.2.1, https://CRAN.R-project.org/package=ggtern

Hampson, G.J. 1997. A sequence stratigraphic model for deposition of the Lower Kinderscout Delta, an Upper Carboniferous turbidite-fronted delta. *Proceedings of the Yorkshire Geological and Polytechnic Society*, **51**, 273–296, https://doi.org/10.1144/pygs.51.4.273

Hennissen, J.A.I., Hough, E. *et al*. 2017. The prospectivity of a potential shale gas play: an example from the southern Pennine Basin (central England, UK). *Marine and Petroleum Geology*, **86**, 1047–1066, https://doi.org/10.1016/j.marpetgeo.2017.06.033

Hennissen, J.A.I., Emmings, J. *et al*. 2024. The Bowland Shale Formation in the Blacon Basin: palaeoecology and resource potential. *Geological Society, London, Special Publications*, **534**, https://doi.org/10.1144/SP534-2022-211

Hild, E. and Brumsack, H.J. 1998. Major and minor element geochemistry of Lower Aptian sediments from the NW German Basin (core Hohenegglesen KB 40). *Cretaceous Research*, **19**, 615–633, https://doi.org/10.1006/cres.1998.0122

Holdsworth, B. and Collinson, J.D. 1988. Millstone Grit cyclicity revisited. *In*: Besly, B.M. and Kelling, G. (eds) *Sedimentation in a Synorogenic Basin Complex: The Upper Carboniferous of Northwest Europe*. Blackie, Glasgow, 132–152.

Hollis, C. and Walkden, G. 2012. Burial diagenetic evolution of the Lower Carboniferous (Dinantian) of the southern margin of the Askrigg Platform and a comparison with the Derbyshire Platform. *Petroleum Geoscience*, **18**, 83–95, https://doi.org/10.1144/1354-079311-049

IPCC. 2014. *Climate Change 2014: Synthesis Report. Contribution of Working Groups I, II and III to the Fifth Assessment Report of the Intergovernmental Panel on Climate Change*. IPCC, Geneva, Switzerland.

Jackson, D.I., Johnson, H. and Smith, N.J.P. 1997. Stratigraphical relationships and a revised lithostratigraphical nomenclature for the Carboniferous, Permian and Triassic rocks of the offshore East Irish Sea Basin. *Geological Society, London, Special Publications*, **124**, 11–32, https://doi.org/10.1144/GSL.SP.1997.124.01.02

Jarvie, D.M. 2012*a*. Shale resource systems for oil and gas: part 1 – shale-gas resource systems. *AAPG Memoirs*, **97**, https://doi.org/10.1306/13321446M973489

Jarvie, D.M. 2012*b*. Shale resource systems for oil and gas: part 2 – shale-oil resource systems. *AAPG Memoirs*, **97**, https://doi.org/10.1306/13321447M973489

Juerges, A., Hollis, C.E., Marshall, J. and Crowley, S. 2016. The control of basin evolution on patterns of sedimentation and diagenesis: an example from the Mississippian Great Orme, North Wales. *Journal of the Geological Society, London*, **173**, 438–456, https://doi.org/10.1144/jgs2014-149

Kabanov, P. and Jiang, C. 2020. Photic-zone euxinia and anoxic events in a Middle-Late Devonian shelfal sea of Panthalassan continental margin, NW Canada: changing paradigm of Devonian ocean and sea level fluctuations. *Global and Planetary Change*, **188**, 103153, https://doi.org/10.1016/j.gloplacha.2020.103153

Kampschulte, A. and Strauss, H. 2004. The sulfur isotopic evolution of Phanerozoic seawater based on the analysis of structurally substituted sulfate in carbonates. *Chemical Geology*, **204**, 255–286, https://doi.org/10.1016/j.chemgeo.2003.11.013

Kampschulte, A., Bruckschen, P. and Strauss, H. 2001. The sulphur isotopic composition of trace sulphates in Carboniferous brachiopods: implications for coeval seawater, correlation with other geochemical cycles and isotope stratigraphy. *Chemical Geology*, **175**, 149–173, https://doi.org/10.1016/S0009-2541(00)00367-3

Kendrick, M.A., Burgess, R., Pattrick, R.A.D. and Turner, G. 2002. Hydrothermal fluid origins in a fluorite-rich Mississippi Valley-Type District: combined noble gas (He, Ar, Kr) and halogen (Cl, Br, I) analysis of fluid inclusions from the South Pennine Ore Field, United Kingdom. *Economic Geology*, **97**, 435–451, https://doi.org/10.2113/gsecongeo.97.3.435

Kerschke, D. and Schulz, H.-M. 2013. The shale gas potential of Tournaisian, Visean, and Namurian black shales in North Germany: baseline parameters in a geological context. *Environmental Earth Sciences*, **70**, 3817–3837, https://doi.org/10.1007/s12665-013-2745-9

Kidder, D.L. and Worsley, T.R. 2010. Phanerozoic Large Igneous Provinces (LIPs), HEATT (Haline Euxinic Acidic Thermal Transgression) episodes, and mass extinctions. *Palaeogeography, Palaeoclimatology, Palaeoecology*, **295**, 162–191, https://doi.org/10.1016/j.palaeo.2010.05.036

Kirkham, A. 2021. Mass collapse and resedimentation on a Brigantian–Early Namurian platform margin, Halkyn–Mold area, North Wales, UK. *Geological Journal*, **56**, 3672–3686, https://doi.org/10.1002/gj.4127

Könitzer, S.F., Davies, S., Stephenson, M. and Leng, M. 2014. Depositional controls on mudstone lithofacies in a basinal setting: implications for the delivery of sedimentary organic matter. *Journal of Sedimentary Research*, **84**, 198–214, https://doi.org/10.2110/jsr.2014.18

Könitzer, S.F., Stephenson, M.H., Davies, S.J., Vane, C.H. and Leng, M.J. 2016. Significance of sedimentary organic matter input for shale gas generation potential of Mississippian Mudstones, Widmerpool Gulf, UK. *Review of Palaeobotany and Palynology*, **224**, 146–168, https://doi.org/10.1016/j.revpalbo.2015.10.003

Kuhn, M. 2020. *Caret* R package version 6.0-86, https://CRAN.R-project.org/package=caret

Lafargue, E., Marquis, F. and Pillot, D. 1998. Rock-Eval 6 applications in hydrocarbon exploration, production, and soil contamination studies. *Revue de l'Institut Francais du Petrole*, **53**, 421–437, https://doi.org/10.2516/ogst:1998036

Lecomte, A., Cathelineau, M., Michels, R., Peiffert, C. and Brouand, M. 2017. Uranium mineralization in the Alum Shale Formation (Sweden): evolution of a U-rich marine black shale from sedimentation to metamorphism. *Ore Geology Reviews*, **88**, 71–98, https://doi.org/10.1016/j.oregeorev.2017.04.021

Lee, M.K., Brown, G.C., Webb, P.C., Whieldon, J. and Rollin, K.E. 1987. Heat flow, heat production and thermo-tectonic setting in mainland UK. *Journal of the Geological Society, London*, **144**, 35–42, https://doi.org/10.1144/gsjgs.144.1.0035

Leeder, M.R. 1982. Upper Palaeozoic basins of the British Isles – Caledonide inheritance versus Hercynian plate margin processes. *Journal of the Geological Society, London*, **139**, 479–491, https://doi.org/10.1144/gsjgs.139.4.0479

Leeder, M., Raiswell, R., Al-Biatty, H., Mcmahon, A. and Hardman, M. 1990. Carboniferous stratigraphy, sedimentation and correlation of well 48/3-3 in the southern North Sea Basin: integrated use of palynology, natural gamma/sonic logs and carbon/sulphur geochemistry. *Journal of the Geological Society, London*, **147**, 287–300, https://doi.org/10.1144/gsjgs.147.2.0287

Lewan, M.D. 1986. Stable carbon isotopes of amorphous kerogens from Phanerozoic sedimentary rocks. *Geochimica et Cosmochimica Acta*, **50**, 1583–1591, https://doi.org/10.1016/0016-7037(86)90121-3

Lindgreen, H. 1994. Ammonium fixation during illite-smectite diagenesis in Upper Jurassic shale, North Sea. *Clay Minerals*, **29**, 527–537, https://doi.org/10.1180/claymin.1994.029.4.10

Loucks, R. and Ruppel, S. 2007. Mississippian Barnett Shale: lithofacies and depositional setting of a deep-water shale-gas succession in the Fort Worth Basin, Texas. *AAPG Bulletin*, **91**, 579–601, https://doi.org/10.1306/11020606059

Loveless, S.E., Bloomfield, J.P. *et al*. 2018. Characterising the vertical separation of shale-gas source rocks and aquifers across England and Wales (UK). *Hydrogeology Journal*, **26**, 1975–1987, https://doi.org/10.1007/s10040-018-1737-y

Magraw, D. and Ramsbottom, W.H.C. 1957. A deep borehole for oil at Croxteth Park, near Liverpool. *Geological Journal*, **1**, 512–535, https://doi.org/10.1002/gj.3350010605

Martinsen, O.J., Collinson, J.D. and Holdsworth, B.K. 1995. Millstone Grit cyclicity revisited, II: sequence stratigraphy and sedimentary responses to changes of relative sea-level. *In*: Plint, G.A. (ed.) *Sedimentary Facies Analysis*. Blackwell Publishing, 305–327.

Maynard, J.R. and Leeder, M.R. 1992. On the periodicity and magnitude of Late Carboniferous glacio-eustatic sea-level changes. *Journal of the Geological Society, London*, **149**, 303–311, https://doi.org/10.1144/gsjgs.149.3.0303

Maynard, J.R., Wignall, P.B. and Varker, W.J. 1991. A 'hot' new shale facies from the Upper Carboniferous of Northern England. *Journal of the Geological Society, London*, **148**, 805–808, https://doi.org/10.1144/gsjgs.148.5.0805

Mazzini, A., Ivanov, M.K. *et al*. 2004. Methane-related authigenic carbonates from the Black Sea: geochemical characterisation and relation to seeping fluids. *Marine Geology*, **212**, 153–181, https://doi.org/10.1016/j.margeo.2004.08.001

Mehra, A., Keller, B. *et al*. 2021. Curation and analysis of global sedimentary geochemical data to inform Earth history. *GSA Today*, **31**, https://doi.org/10.1130/GSATG484A.1

Mercuzot, M., Thomazo, C. *et al*. 2021. Carbon and nitrogen cycle dynamic in continental late-Carboniferous to early Permian basins of Eastern Pangea (Northeastern Massif Central, France). *Frontiers in Earth Science*, **9**, https://doi.org/10.3389/feart.2021.705351

Meyer, K.M. and Kump, L.R. 2008. Oceanic euxinia in earth history: causes and consequences. *Annual Review of Earth and Planetary Sciences*, **36**, 251–288, https://doi.org/10.1146/annurev.earth.36.031207.124256

Meyers, P.A. 1994. Preservation of elemental and isotopic source identification of sedimentary organic matter. *Chemical Geology*, **114**, 289–302, https://doi.org/10.1016/0009-2541(94)90059-0

Midttømme, K. and Roaldset, E. 1999. Thermal conductivity of sedimentary rocks: uncertainties in measurement and modelling. *Geological Society, London, Special Publications*, **158**, 45–60, https://doi.org/10.1144/GSL.SP.1999.158.01.04

Midttømme, K., Roaldset, E. and Aagaard, P. 1998. Thermal conductivity of selected claystones and mudstones from England. *Clay Minerals*, **33**, 131–145, https://doi.org/10.1180/000985598545327

Miles, J.C., Appleton, J.D. *et al*. 2007. *Indicative Atlas of Radon in England and Wales*. Health Protection Agency and the British Geological Survey Report **HPA-RPD-033**.

Mitchum, R.M. and Van Wagoner, J.C. 1991. High-frequency sequences and their stacking patterns: sequence-stratigraphic evidence of high-frequency eustatic cycles. *Sedimentary Geology*, **70**, 131–160, https://doi.org/10.1016/0037-0738(91)90139-5

Monaghan, A.A., Underhill, J.R., Marshall, J.E.A. and Hewett, A.J. 2019. Paleozoic plays of NW Europe: an introduction. *Geological Society, London, Special*

Publications, **471**, 1–15, https://doi.org/10.1144/SP471.13

Morton, A., Waters, C., Fanning, M., Chisholm, I. and Brettle, M. 2015. Origin of Carboniferous sandstones fringing the northern margin of the Wales-Brabant Massif: insights from detrital zircon ages. *Geological Journal*, **50**, 553–574, https://doi.org/10.1002/gj.2572

Mossmann, J.-R., Aplin, A.C., Curtis, C.D. and Coleman, M.L. 1991. Geochemistry of inorganic and organic sulphur in organic-rich sediments from the Peru Margin. *Geochimica et Cosmochimica Acta*, **55**, 3581–3595, https://doi.org/10.1016/0016-7037(91)90057-C

Nash, T. 1979. *Uranium and Thorium in Granitic Rocks of Northeastern Washington and Northern Idaho, with Comments on Uranium Resource Potential*. USGS Open-File Report **79-233**.

Newport, L.P., Aplin, A.C., Gluyas, J.G., Greenwell, H.C. and Gröcke, D.R. 2016. Geochemical and lithological controls on a potential shale reservoir: Carboniferous Holywell Shale, Wales. *Marine and Petroleum Geology*, **71**, 198–210, https://doi.org/10.1016/j.marpetgeo.2015.11.026

Newport, S.M. 2019. *The Bowland Shale (UK): Development of New Sedimentological and Diagenetic Models for a Palaeozoic Fine-Grained Succession*. PhD thesis, University of Manchester.

Newport, S.M., Jerrett, R.M., Taylor, K.G., Hough, E. and Worden, R.H. 2018. Sedimentology and microfacies of a mud-rich slope succession: in the Carboniferous Bowland Basin, NW England (UK). *Journal of the Geological Society, London*, **175**, 247–262, https://doi.org/10.1144/jgs2017-036

Nunn, J.A. and Lin, G. 2002. Insulating effect of coals and organic rich shales: implications for topography-driven fluid flow, heat transport, and genesis of ore deposits in the Arkoma Basin and Ozark Plateau. *Basin Research*, **14**, 129–145, https://doi.org/10.1046/j.1365-2117.2002.00172.x

Nunn, J.A., Lin, G. and Zhang, L. 1999. Thermal insulation by low thermal conductivity shales: implications for basin-scale fluid flow and heat transport. *In*: Förster, A. and Merriam, D.F. (eds) *Geothermics in Basin Analysis*. Springer US, Boston, MA, 117–130.

Palci, F., Fraser, A.J. *et al*. 2020. Shale oil and gas resource evaluation through 3D basin and petroleum systems modelling: a case study from the East Midlands, onshore UK. *Petroleum Geoscience*, **26**, 525–543, https://doi.org/10.1144/petgeo2019-069

Parkes, D., Busby, J., Kemp, S.J., Petitclerc, E. and Mounteney, I. 2021. The thermal properties of the Mercia Mudstone Group. *Quarterly Journal of Engineering Geology and Hydrogeology*, **54**, https://doi.org/10.1144/qjegh2020-098

Parnell, J. and Swainbank, I. 1990. Pb-Pb dating of hydrocarbon migration into a bitumen-bearing ore deposit, North Wales. *Geology*, **18**, 1028–1030, https://doi.org/10.1130/0091-7613(1990)018<1028:PPDOHM>2.3.CO;2

Parnell, J., Brolly, C., Spinks, S. and Bowden, S. 2016. Selenium enrichment in Carboniferous Shales, Britain and Ireland: problem or opportunity for shale gas extraction? *Applied Geochemistry*, **66**, 82–87, https://doi.org/10.1016/j.apgeochem.2015.12.008

Parnell, J., Nkoko, K., Feldmann, J. and Armstrong, J. 2022. Speciation of trace elements in the Bowland Shale. *Geological Society, London, Special Publications*, **534**, https://doi.org/10.1144/SP534-2020-195

Patruno, S. and Helland-Hansen, W. 2018. Clinoforms and clinoform systems: review and dynamic classification scheme for shorelines, subaqueous deltas, shelf edges and continental margins. *Earth-Science Reviews*, **185**, 202–233, https://doi.org/10.1016/j.earscirev.2018.05.016

Pearce, T.J., McLean, D., Martin, J.H., Ratcliffe, K. and Wray, D. 2010. A whole-rock geochemical approach to the recognition and correlation of 'marine bands. *SEPM Special Publications*, **94**, 221–238.

Pellegrini, C., Maselli, V. *et al*. 2017. How to make a 350-m-thick lowstand systems tract in 17 000 years: the Late Pleistocene Po River (Italy) lowstand wedge. *Geology*, **45**, 327–330, https://doi.org/10.1130/G38848.1

Peters-Kottig, W., Strauss, H. and Kerp, H. 2006. The land plant $\delta^{13}C$ record and plant evolution in the Late Palaeozoic. *Palaeogeography, Palaeoclimatology, Palaeoecology*, **240**, 237–252, https://doi.org/10.1016/j.palaeo.2006.03.051

Peters, S. and Loss, D. 2012. Storm and fair-weather wave base: a relevant distinction? *Geology*, **40**, 511–514, https://doi.org/10.1130/G32791.1

Phan, T.T., Capo, R.C. *et al*. 2015. Trace metal distribution and mobility in drill cuttings and produced waters from Marcellus Shale gas extraction: uranium, arsenic, barium. *Applied Geochemistry*, **60**, 89–103, https://doi.org/10.1016/j.apgeochem.2015.01.013

Pharaoh, T.C., Gent, C.M.A. *et al*. 2019. An overlooked play? Structure, stratigraphy and hydrocarbon prospectivity of the Carboniferous in the East Irish Sea–North Channel basin complex. *Geological Society, London, Special Publications*, **471**, 281–316, https://doi.org/10.1144/SP471.7

Pharaoh, T., Haslam, R. *et al*. 2020. The Môn-Deemster-Ribblesdale Fold-Thrust Belt, Central UK: a concealed Variscan inversion belt located on weak Caledonian crust. *Geological Society, London, Special Publications*, **490**, 153–176, https://doi.org/10.1144/SP490-2018-109

R, Core Team 2018. *R: a language and environment for statistical computing*. R Foundation for Statistical Computing, Vienna, Austria, https://www.R-project.org

Raiswell, R. and Berner, R.A. 1987. Organic carbon losses during burial and thermal maturation of normal marine shales. *Geology*, **15**, 853–856, https://doi.org/10.1130/0091-7613(1987)15<853:OCLDBA>2.0.CO;2

Ramsbottom, W.H.C. 1977. Major cycles of transgression and regression (mesothems) in the Namurian. *Proceedings of the Yorkshire Geological and Polytechnic Society*, **41**, 261–291, https://doi.org/10.1144/pygs.41.3.261

Ramsbottom, W.H.C. 1979. Rates of transgression and regression in the Carboniferous of NW Europe. *Journal of the Geological Society, London*, **136**, 147–153, https://doi.org/10.1144/gsjgs.136.2.0147

Ramsbottom, W.H.C. and Saunders, W.B. 1985. Evolution and evolutionary biostratigraphy of Carboniferous ammonoids. *Journal of Paleontology*, **59**, 123–139.

Ramsbottom, W.H.C., Rhys, G.J. and Smith, E.G. 1962. Boreholes in the Carboniferous rocks of the Ashover district, Derbyshire. *Bulletin of the Geological Survey of Great Britain*, **19**, 75–168.

Riley, D.A., Pearce, T.J., Mathia, E., Ratcliffe, K. and Martin, J. 2018. The application of elemental geochemistry to UK onshore unconventional plays. *Geological Society, London, Petroleum Geology Conference Series*, **8**, 585–594, https://doi.org/10.1144/PGC8.8

Rollin, K. 2002. *Assessment of BGS Data for Ground Source Heat Pump Installations in the UK*. British Geological Survey Internal Report **IR/02/196**.

Rutqvist, J. 2020. Thermal management associated with geologic disposal of large spent nuclear fuel canisters in tunnels with thermally engineered backfill. *Tunnelling and Underground Space Technology*, **102**, 103454, https://doi.org/10.1016/j.tust.2020.103454

Rybach, L. 1976. Radioactive heat production: a physical property determined by the chemistry of rocks. *In*: Strens, R.G.J. (ed.) *The Physics and Chemistry of Minerals and Rocks*. Wiley, London, 309–318.

Rygel, M.C., Fielding, C.R., Frank, T.D. and Birgenheier, L.P. 2008. The magnitude of late Paleozoic glacioeustatic fluctuations: a synthesis. *Journal of Sedimentary Research*, **78**, 500–511, https://doi.org/10.2110/jsr.2008.058

Saunders, W.B. and Ramsbottom, W.H.C. 1986. The mid-Carboniferous eustatic event. *Geology*, **14**, 208–212, https://doi.org/10.1130/0091-7613(1986)14<208:TMEE>2.0.CO;2

Schuster, A., Strehlow, B.W., Eckford-Soper, L., McAllen, R. and Canfield, D.E. 2021. Effects of seasonal anoxia on the microbial community structure in demosponges in a Marine Lake in Lough Hyne, Ireland. *mSphere*, **6**, e00991–e009920, https://doi.org/10.1128/mSphere.00991-20

Shanmugam, G. and Moiola, R.J. 1982. Eustatic control of turbidites and winnowed turbidites. *Geology*, **10**, 231–235, https://doi.org/10.1130/0091-7613(1982)10<231:ECOTAW>2.0.CO;2

Sims, M.J.E., Sephton, M.A., Watson, J.S., Fraser, A.J. and Vane, C.H. 2024. Biomarker evidence for the depositional environment of basinal UK Mississippian mudstones. *Geological Society, London, Special Publications*, **534**, https://doi.org/10.1144/SP534-2022-225

Smedley, P.L., Smith, B., Abesser, C. and Laptworth, D. 2006. *Uranium Occurrence and Behaviour in British Groundwater*. British Geological Survey Commissioned Report **CR/06/050N**.

Smith, N., Kirby, G.A., Pharaoh, T.C., Hulbert, A.G. and Shaw, K. 2005. *Structure and Evolution of the South-West Pennine Basin and Adjacent Area*. British Geological Survey.

Somerville, I.D. 1979. A cyclicity in the early Brigantian (D2) limestones east of the Clwydian Range, North Wales and its use in correlation. *Geological Journal*, **14**, 69–86, https://doi.org/10.1002/gj.3350140105

Spears, D.A., Kanaris-Sotiriou, R., Riley, N. and Krause, P. 1999. Namurian bentonites in the Pennine Basin, UK – origin and magmatic affinities. *Sedimentology*, **46**, 385–401, https://doi.org/10.1046/j.1365-3091.1999.00220.x

Talling, P., Masson, D., Sumner, E. and Malgesini, G. 2012. Subaqueous sediment density flows: depositional processes and deposit types. *Sedimentology*, **59**, 1937–2003, https://doi.org/10.1111/j.1365-3091.2012.01353.x

Taylor, S. and McLennan, S. 1985. *The Continental Crust: Its Composition and Evolution*. Blackwell Scientific.

Tissot, B. and Welte, D. 1984. *Petroleum Formation and Occurrence*. Springer.

Tribovillard, N. 2020. Arsenic in marine sediments: how robust a redox proxy? *Palaeogeography, Palaeoclimatology, Palaeoecology*, **550**, 109745, https://doi.org/10.1016/j.palaeo.2020.109745

Tribovillard, N., Algeo, T., Lyons, T. and Riboulleau, A. 2006. Trace metals as paleoredox and paleoproductivity proxies: an update. *Chemical Geology*, **232**, 12–32, https://doi.org/10.1016/j.chemgeo.2006.02.012

Tribovillard, N., Algeo, T.J., Baudin, F. and Riboulleau, A. 2012. Analysis of marine environmental conditions based on molybdenum–uranium covariation – applications to Mesozoic paleoceanography. *Chemical Geology*, **324–325**, 46–58, https://doi.org/10.1016/j.chemgeo.2011.09.009

Tyson, R. (ed.) 1995. *Sedimentary Organic Matter: Organic Facies and Palynofacies*. Chapman and Hall, London.

van de Velde, S.J., Reinhard, C.T., Ridgwell, A. and Meysman, F.J.R. 2020. Bistability in the redox chemistry of sediments and oceans. *Proceedings of the National Academy of Sciences*, **117**, 33043–33050, https://doi.org/10.1073/pnas.2008235117

van den Boogaart, G., Tolosana-Delgado, R. and Bren, M. 2020. *Compositions* R package version 2.0-0, https://CRAN.R-project.org/package=compositions

Van Mooy, B.A.S., Keil, R.G. and Devol, A.H. 2002. Impact of suboxia on sinking particulate organic carbon: enhanced carbon flux and preferential degradation of amino acids via denitrification. *Geochimica et Cosmochimica Acta*, **66**, 457–465, https://doi.org/10.1016/S0016-7037(01)00787-6

Veevers, J.J. and Powell, C.M. 1987. Late Paleozoic glacial episodes in Gondwanaland reflected in transgressive-regressive depositional sequences in Euramerica. *GSA Bulletin*, **98**, 475–487, https://doi.org/10.1130/0016-7606(1987)98<475:LPGEIG>2.0.CO;2

Vilà, M., Fernández, M. and Jiménez-Munt, I. 2010. Radiogenic heat production variability of some common lithological groups and its significance to lithospheric thermal modeling. *Tectonophysics*, **490**, 152–164, https://doi.org/10.1016/j.tecto.2010.05.003

Warr, L.N. 2000. The Variscan Orogeny: the welding of Pangaea. *In*: Woodcock, N.H. and Strachan, R. (eds) *Geological History of Britain and Ireland*. Wiley-Blackwell, Hoboken, USA, 271–294.

Warren, P.T., Price, D. *et al*. 1984. *Geology of the Country Around Rhyl and Denbigh, Memoir for 1:50 000 Geological Sheets 95 and 107 and Parts of Sheets 94 and 106*. Memoirs of the Geological Survey of Great Britain, England and Wales (Sheet – New Series). HMSO, London.

Waters, C.N. and Condon, D.J. 2012. Nature and timing of Late Mississippian to Mid-Pennsylvanian glacio-eustatic sea-level changes of the Pennine Basin, UK.

Journal of the Geological Society, London, **169**, 37–51, https://doi.org/10.1144/0016-76492011-047

Waters, C.N. and Davies, S.J. 2006. Carboniferous: extensional basins, advancing deltas and coal swamps. *In*: Brenchley, P.J. (ed.) *The Geology of England and Wales*. Geological Society, London, 173–223.

Waters, C.N., Browne, M.A.E., Dean, M.T. and Powell, J.H. 2007. *Lithostratigraphical Framework for Carboniferous Successions of Great Britain (Onshore)*. British Geological Survey Research Report **RR/07/01**.

Waters, C.N., Waters, R.A., Barclay, W.J. and Davies, J.R. 2009. *A Lithostratigraphical Framework for the Carboniferous Successions of Southern Great Britain (Onshore)*. British Geological Survey Research Report **RR/09/01**.

Waters, C.N., Somerville, I.D. *et al*. 2011. *A Revised Correlation of Carboniferous Rocks in the British Isles*. Geological Society, London.

Waters, C.N., Vane, C.H. *et al*. 2020. Lithological and chemostratigraphic discrimination of facies within the Bowland Shale Formation within the Craven and Edale basins, UK. *Petroleum Geoscience*, **26**, 325–345, https://doi.org/10.1144/petgeo2018-039

Waters, C.N., Morton, A. and Frei, D. 2021. Interplay of southern, western, and northern sources during deposition of North Wales Carboniferous sandstones, determined from heavy minerals, mineral chemistry, and detrital zircon ages. *Geological Journal*, **56**, 2699–2719, https://doi.org/10.1002/gj.4063

Wei, W. and Algeo, T.J. 2020. Elemental proxies for paleosalinity analysis of ancient shales and mudrocks. *Geochimica et Cosmochimica Acta*, **287**, 341–366, https://doi.org/10.1016/j.gca.2019.06.034

Whitelaw, P., Uguna, C.N. *et al*. 2019. Shale gas reserve evaluation by laboratory pyrolysis and gas holding capacity consistent with field data. *Nature Communications*, **10**, 3659, https://doi.org/10.1038/s41467-019-11653-4

Wickham, H. 2009. *ggplot2: Elegant Graphics for Data Analysis*. Springer-Verlag, New York.

Wickham, H. and Francois, R. 2016. *dplyr* R package version 0.5.0, https://CRAN.R-project.org/package=dplyr

Wignall, P.B. 1994. *Black Shales*. Clarendon Press; Oxford University Press, Oxford.

Williams, G.D. and Eaton, G.P. 1993. Stratigraphic and structural analysis of the Late Palaeozoic–Mesozoic of NE Wales and Liverpool Bay: implications for hydrocarbon prospectivity. *Journal of the Geological Society, London*, **150**, 489–499, https://doi.org/10.1144/gsjgs.150.3.0489

Worden, R.H., Allen, M.J. *et al*. 2020. Lower Cretaceous Rodby and Palaeocene Lista Shales: characterisation and comparison of top-seal mudstones at two planned CCS sites, Offshore UK. *Minerals*, **10**, 691, https://doi.org/10.3390/min10080691

Zeileis, A. and Grothendieck, G. 2005. Zoo: S3 infrastructure for regular and irregular time series. *Journal of Statistical Software*, **14**, 1–27, https://doi.org/10.18637/jss.v014.i06

Zijp, M., Nelskamp, S. and Doornenbal, H. 2017. *Resource Estimation of Shale Gas and Shale Oil in Europe*. Report T7b of the EUOGA study (EU Unconventional Oil and Gas Assessment) commissioned by European Commission Joint Research Centre to GEUS.